Chronic Mcm10 deficiency causes defects in telomere maintenance in human cells

Ryan M. Baxley[1], Wendy Leung[1,4], Jacob Peter Matson[2,4], Marissa K. Oram[1], Megan M. Schmit[1], Liangjun Wang[1], Jack Hedberg[1], Colette B. Rogers[1], Adam J. Harvey[1], Debashree Basu[1], Eric A. Hendrickson[1], Emily M. Mace[3], Jordan S. Orange[3], Jeanette Gowen Cook[2] and Anja-Katrin Bielinsky[1,5,*]

[1]Department of Biochemistry, Molecular Biology, and Biophysics, University of Minnesota, Minneapolis, MN 55455, USA

[2]Department of Biochemistry and Biophysics, University of North Carolina, Chapel Hill, NC 27599, USA

[3]Vagelos College of Physicians and Surgeons, Columbia University, New York, NY 10032, USA

[4]These authors contributed equally

[5]Lead Contact

[*]Correspondence: bieli003@umn.edu

Summary

Minichromosome maintenance protein 10 (Mcm10) is essential for eukaryotic DNA replication initiation and fork stability. Recently, a compound heterozygous *MCM10* mutation was identified in a patient who presented with natural killer (NK) cell deficiency. To understand the mechanism of disease, we modeled this mutation in human cell lines. We demonstrate that Mcm10 deficiency causes chronic replication stress that reduces cell viability due to increased genomic instability and telomere maintenance defects. Our data suggests that Mcm10 deficiency constrains telomerase-dependent telomere extension. This limitation can be overcome by increasing telomerase activity, although defects in telomere replication persist. We propose that stalled replication forks in Mcm10-deficient cells arrest terminally, especially within hard-to-replicate regions, and require nuclease processing involving Mus81, as *MCM10*:*MUS81* double mutants displayed decreased viability and accelerated telomere erosion. Our results reveal that Mcm10 is critical for telomere replication and provide insights into how *MCM10* mutations cause NK cell deficiency.

Introduction

A robust DNA replication program has evolved to ensure genome duplication without major sequence mutations, deletions or rearrangements. Conceptually, this program can be divided into three phases: origin licensing, origin firing and DNA synthesis. Licensing occurs during late mitosis and G1-phase to load double hexamers of the core replicative helicase, composed of minichromosome maintenance complex proteins 2-7 (Mcm2-7), onto double-stranded (ds) DNA (Evrin et al., 2009, Remus et al., 2009). After origin licensing, which usually occurs in significant excess of what is minimally required for complete genome duplication, cells transition from G1- to S-phase and initiate replication (Bielinsky, 2003, Blow et al., 2011). This requires helicase co-activators, including the go-ichi-ni-san (GINS) complex and cell division cycle protein 45 (Cdc45), to form the Cdc45-Mcm2-7-GINS (CMG) helicase (Moyer et al., 2006, Yeeles et al., 2015). Upon firing, CMG complexes reconfigure and bypass each other to unwind dsDNA bi-directionally (Douglas et al., 2018, Langston and O'Donnell, 2019). Origin firing events occur throughout the genome as S-phase progresses to complete duplication prior to cell division (Boos and Ferreira, 2019).

Origin firing requires recruitment of minichromosome maintenance protein 10 (Mcm10) (Langston and O'Donnell, 2019, Thu and Bielinsky, 2013, Yeeles et al., 2015), and the protein remains associated with the CMG complex to promote replication elongation (Looke et al., 2017, Watase et al., 2012). Yeast Mcm10 aids in the bypass of lagging strand blocks and protects stalled forks by regulating fork regression (Langston et al., 2017, Mayle et al., 2019). Consistent with these observations, Mcm10 is critical for replisome stability (Chadha et al., 2016). Given these functions, it is not surprising

that loss of Mcm10 causes replication stress, DNA damage and cell cycle arrest (Baxley and Bielinsky, 2017).

Several endogenous and exogenous sources produce replication stress that disrupts DNA synthesis, generating aberrant fork structures and single-stranded (ss) DNA gaps. An unavoidable source of endogenous replication stress is encountered in hard-to-replicate regions, including common fragile sites (CFSs) and telomeres, which are origin-poor loci and contain repetitive DNA sequences (Debatisse et al., 2012, Sfeir et al., 2009). Telomeres present many challenges to replisome progression including the propensity to form G-quadruplexes, R- and telomere-loops (t-loop) (Maestroni et al., 2017, Mason-Osann et al., 2019). Telomere replication not only requires canonical replisome proteins, but is facilitated by components of the Shelterin complex, DNA helicases, homologous recombination and DNA repair factors (Martinez and Blasco, 2015, Pan et al., 2017, Schmutz et al., 2017, Vannier et al., 2012). In contrast, the alternative lengthening of telomeres (ALT) pathway relies heavily on break-induced replication and has defined features that are distinct from telomere maintenance in telomerase-positive cells (Dilley et al., 2016, Sobinoff et al., 2017, Zhang et al., 2019). The vast majority of human cancers achieve immortalization by reactivating telomerase (Jafri et al., 2016), suggesting that a comprehensive understanding of telomere replication and its role in human disease requires further studies in telomerase-positive cancer cell models.

In cancer cell lines and tumor samples *MCM10* is commonly upregulated (Cui et al., 2018, Senfter et al., 2017, Wang et al., 2019). As Mcm10 depletion causes incomplete replication and DNA damage, cancer cells may rely on Mcm10 to prevent

genomic instability from reaching lethal levels (Baxley and Bielinsky, 2017). Recently, hypomorphic mutations in *MCM10* were associated with a different pathology. A patient carrying a compound heterozygous *MCM10* mutation in the germline was recently described to present with natural killer (NK) cell deficiency (NKD) (Mace et al., bioRxiv doi: 10.1101/825554, 2019). The mutant alleles carried a missense (c.C1276T, p.R426C) and nonsense mutation (c.C1744T, p.R582X), respectively, which blocked NK cell maturation in the patient (Mace et al., bioRxiv doi: 10.1101/825554, 2019). The causative role of these mutations in NKD is strengthened by an emerging connection between NKD and replication gene mutations. Indeed, NKD-associated mutations in *MCM4* and *GINS1* increased replication stress and caused genomic instability, similar to loss of *MCM10* function, and resulted in incomplete NK cell development (Casey et al., 2012, Cottineau et al., 2017, Gineau et al., 2012, Hughes et al., 2012). Thus, to elucidate the mechanism of *MCM10*-associated NKD, we generated human cell lines harboring mutations mimicking those of the patient.

In this study, we demonstrate that human *MCM10* is haploinsufficient in transformed HCT116 and non-transformed hTERT RPE-1 cells, as inactivating a single allele of the gene caused mutant phenotypes. These phenotypes were more severe in HCT116 cells, disrupting normal cell cycle distribution and affecting global DNA synthesis due to decreased origin firing. Both cell types displayed increased cell death and disrupted telomere length maintenance although telomerase activity was unaltered. *MCM10* mutants showed significant defects in telomere replication and accumulated telomeric "t-complex" DNA comprised of highly branched structures containing internal ssDNA gaps that arose from stalled forks. We argue that this altered telomere structure

5

compromised telomerase access to chromosome ends. Telomere erosion was not a characteristic of *CDC45* or *MCM4* haploinsufficiency, suggesting that unlike Mcm10 deficiency, chronic reduction of Cdc45 or Mcm4 did not limit telomere replication. Finally, our data demonstrate that stalled forks required nuclease processing to prevent fork collapse, as *MCM10:MUS81* double mutants displayed exacerbated phenotypes. Taken together, our results reveal that Mcm10 is critical for human telomere replication and provide insights into how *MCM10* mutations could cause NK cell deficiency.

Results

Inactivation of a single *MCM10* allele in HCT116 cells reveals haploinsufficiency

We hypothesized that the patient *MCM10* nonsense mutation was the main contributor causing NKD. To model this mutation, we utilized rAAV-mediated gene targeting of *MCM10* exon 14 in HCT116 cells (Figure 1A). The nonsense mutation or deletion of exon 14 each introduced premature stop codons and presumably led to nonsense-mediated decay of the mRNA. Regardless, if translated, these mutations would truncate Mcm10 at amino acid 582 or 583, respectively, prior to the nuclear localization sequence and thus remain cytoplasmic (Sharma et al., 2010). PCR analyses confirmed one knockout allele carrying a *loxP* scar and one functional allele with wild type coding sequence and a 3' *loxP* site (Figure 1B). Western blot analysis demonstrated stable Mcm10 reduction in *MCM10*$^{+/-}$ cell lines (Figure 1C), which significantly slowed cell proliferation (Figure 1D). These observations implied that in HCT116 cells *MCM10* is genetically haploinsufficient.

MCM10 haploinsufficiency was unexpected, as heterozygous mice were healthy and fertile (Lim et al., 2011) and haploinsufficiency is uncommon among human genes (Bartha et al., 2018, Huang et al., 2010). To confirm *MCM10* haploinsufficiency, we used an independent CRISPR-Cas9 gene targeting strategy to introduce inactivating frameshift mutations into exon 3 (Figure 1A) in HCT116 and hTERT RPE-1 cell lines (subsequently referred to as RPE-1). Consistent with analyses of the exon 14 *MCM10*$^{+/-}$ HCT116 mutants, exon 3 *MCM10*$^{+/-}$ HCT116 and RPE-1 cells showed a stable reduction of Mcm10 expression and accordingly slower growth rates (Figure 1C,D,E). Furthermore, the ability of individual *MCM10*$^{+/-}$ HCT116 cells to form colonies was

significantly reduced (Figure 1 F,G). Taken together, our findings uncovered *MCM10* haploinsufficiency in HCT116 and RPE-1 cell lines.

Mcm10 deficiency alters DNA synthesis and cell cycle progression in HCT116 cancer cells

To define the cause of the growth defect in *MCM10*$^{+/-}$ mutants, we utilized quantitative analytical flow cytometry. Cell cycle distribution was assessed using DAPI-staining for DNA content in combination with an EdU pulse to label S-phase cells (Figure 2A). In HCT116 *MCM10*$^{+/-}$ cells, we detected a significant increase in G1- and decrease in S-phase populations (Figure 2B). These data suggested delayed progression through the G1/S-phase transition, which could be attributed to defects in origin licensing, activation, reduced fork speed, DNA damage induced G1-arrest or a combination thereof. To delineate among these possibilities, we measured chromatin bound Mcm2 and EdU labeled DNA to quantify G1-phase licensing and S-phase DNA synthesis (Figure 2C,D) (Matson et al., 2017). Origin licensing in *MCM10*$^{+/-}$ mutants was identical to wild type cells (Figure 2E). However, we observed a significant DNA synthesis defect during the 30-minute labeling pulse in *MCM10*$^{+/-}$ cells (Figure 2F). These data demonstrated a requirement for Mcm10 in DNA synthesis, but not origin licensing, and are consistent with the published roles for Mcm10 in DNA replication (Baxley and Bielinsky, 2017).

We next analyzed cell cycle distribution and DNA synthesis in *MCM10*$^{+/-}$ RPE-1 cells. A significant change in the cell cycle distribution of *MCM10*$^{+/-}$ cells was not observed (Figure 2G, H). Furthermore, the amount of origin licensing (Figure 2I,J) and

S-phase DNA synthesis (Figure 2I,K) were normal. The lack of detectable replication phenotypes in $MCM10^{+/-}$ RPE-1 cells was consistent with the smaller decrease in growth rate in comparison to $MCM10^{+/-}$ HCT116 cells (Figure 1D,E). Notably, origin licensing and DNA synthesis were significantly higher in wild type HCT116 than in RPE-1 cells (Figure 2L,M). These data reflect differences between cell types, likely including changes that HCT116 cells underwent during oncogenic transformation, and suggest that transformed cells may be inherently more sensitive to Mcm10 deficiency.

Reduced origin firing causes DNA replication defects and impairs viability of Mcm10-deficient cells

To understand the DNA synthesis defect in $MCM10^{+/-}$ HCT116 cells we performed DNA combing. We first measured inter-origin distance (IOD) to determine if origin firing was perturbed. Whereas wild type cells displayed an average IOD of ~91 kb, the IOD in $MCM10^{+/-}$ cells markedly increased to ~120 kb (Figure 3A,B). This difference equates to ~25% fewer origin firing events in $MCM10$ mutants. Next, we measured global fork speed and stability. Fork speed was modestly, but significantly, increased in $MCM10^{+/-}$ cells (Figure 3A,C) and is consistent with the inverse regulation of fork speed and origin firing reported in eukaryotes (Rodriguez-Acebes et al., 2018, Zhong et al., 2013). Fork stability was not changed (Figure 3D). These data suggested that Mcm10 deficiency primarily affected global DNA synthesis by reducing the number of active forks. To confirm this idea, we assessed PCNA ubiquitination (PCNA-Ub), because this modification at lysine 164 occurs specifically at active forks in response to replication stress (Leung et al., 2018). Because HCT116 cells exhibit intrinsic replication stress,

9

PCNA-Ub is detectable under unperturbed conditions (Figure 3E) (Bianco et al., 2019). To enhance PCNA-Ub, we exposed cells to $40J/m^2$ of UV radiation. As expected, PCNA-Ub was 1.5- to 3-fold higher in wild type cells than in *MCM10*^{+/-} cells under unperturbed conditions and in response to UV (Figure 3E). Furthermore, we observed that phosphorylated RPA32, which binds to ssDNA exposed during replication stress, was elevated in wild type cells in comparison to *MCM10*^{+/-} cells exposed to UV. Therefore, Mcm10 deficiency decreased origin firing and resulted in fewer active forks. However, the majority of forks were stable and did not elicit an increased stress response.

We hypothesized that the reduced proliferation and clonogenic survival of HCT116 *MCM10*^{+/-} cells was partly due to cell death, because slow-growing colonies did not emerge, even when we allowed additional time for them to form (Figure S1A). Flow cytometry analysis of cells stained with propidium iodide (PI) and annexin V confirmed that cell death was increased in *MCM10*^{+/-} populations over wild type (Figure 3F, Figure S1B). We also used MTS assays to evaluate whether genotoxic stress exacerbated the viability defect. Surprisingly, wild type and *MCM10*^{+/-} cells displayed similar sensitivities to hydroxyurea (HU), aphidicolin, cisplatin and etoposide 24-96 h after exposure (Figure S1C). Mitomycin C (MMC) was the only drug tested that significantly decreased *MCM10*^{+/-} cell viability. To assess sensitivity over a longer time period (10-16 days), we performed clonogenic survival assays. Interestingly, *MCM10*^{+/-} cells were significantly more sensitive to UV and MMC, but not HU treatment (Figure 3G). Thus, Mcm10 deficiency caused increased cell death under unperturbed conditions, and certain DNA lesions that require active replisome bypass enhanced this genotoxic stress.

10

Replication stress in Mcm10-deficient cells causes genomic instability and spontaneous reversion of the *MCM10* mutation

To understand if chronic Mcm10 deficiency promoted genome instability, we generated late passage HCT116 wild type and *MCM10$^{+/-}$* populations. As *MCM10$^{+/-}$* cells were passaged, we observed an increase in cells with abnormal morphology and multiple enlarged or pyknotic nuclei indicative of decreased viability (Figure S2A). Karyotype analysis of wild type cells after ~ 200 population doublings (PD) as well as *MCM10$^{+/-}$* populations after mid- (~25 PDs) and late passage (~100 PDs) revealed increased genome instability in the mutants (Figure S2B). Late passage wild type cells harbored three populations represented by the parental HCT116 karyotype and two derivatives, with 10% of karyotypes carrying unique aberrations (Table S1). Mid-passage *MCM10$^{+/-}$* cells were comprised of one major population distinct from the parental karyotype carrying two novel aberrations, as well as seven additional novel karyotypes (Table S1). Overall, 23% of karyotypes had unique aberrations. Furthermore, late passage *MCM10$^{+/-}$* cells consisted of a clonal population distinct from the parental karyotype carrying three novel aberrations, as well as nineteen additional novel karyotypes (Table S1). Overall, 63% of karyotypes had unique aberrations, suggesting that they were the result of independent translocations. The acquired chromosomal rearrangements in *MCM10* mutants significantly overlapped with CFSs (80%; Table S1) (Durkin and Glover, 2007, Lukusa and Fryns, 2008, Mrasek et al., 2010), which is consistent with a role for Mcm10 in preventing fragile site breakage (Miotto et al., 2014).

11

The overlap of translocation hot spots with CFSs prompted us to investigate telomere maintenance, as telomeres are also origin-poor and hard-to-replicate regions (Maestroni et al., 2017, Mason-Osann et al., 2019). We performed telomere restriction fragment (TRF) length analysis to measure average length over time. Whereas wild type telomere length was stable, telomeres in $MCM10^{+/-}$ cell lines were shorter than wild type at early passage and eroded over time (Figure 4A). Consistent with these data, early passage exon 3 $MCM10^{+/-}$ HCT116 cells contained eroded telomeres (Figure S2C). To independently confirm this phenotype, we performed telomere fluorescence *in situ* hybridization (t-FISH) of metaphase chromosomes. Consistent with our TRF analyses we observed a significant increase in chromosomes lacking a telomere signal, termed signal free ends, in $MCM10^{+/-}$ metaphase spreads. We also quantified fragile telomeres, chromosome ends with multiple telomere foci that are indicative of abnormal structure (Sfeir et al., 2009), but did not find any increase in $MCM10^{+/-}$ mutants (Figure 4B). Next, we measured β-galactosidase (β-gal) activity to determine whether $MCM10^{+/-}$ cells activated senescence pathways (Lee and Schmitt, 2019, Shay, 2016). We observed significantly higher activity in mutant cell extracts, further corroborating the telomere maintenance defect (Figure S2D). Finally, we measured telomerase activity using the telomeric repeat amplification protocol (TRAP) (Wright et al., 1995) to ensure that it was equivalent in all cell lines (Figure 4C). We could thus exclude telomerase inactivation as the cause of telomere erosion.

During origin firing, Mcm10-dependent dsDNA unwinding facilitates RPA-loading (Thu and Bielinsky, 2013). Therefore, we examined whether Mcm10's telomere maintenance role was related to the function of the RPA-like complex CST (CTC1-

12

STN1-TEN1). CST promotes telomere replication and coordinates C-strand fill-in following telomerase extension of the G-strand (Stewart et al., 2018). To investigate whether Mcm10 has a role in C-strand fill-in, we utilized G-overhang assays, but did not detect any difference in the G-overhang signal between *MCM10* mutants and wild type cells (Figure S2D,E). As expected, signal increased in conditionally null *CTC1*$^{f/f}$ control cells following Cre-mediated knockout (+4-OHT lanes; Figure S2D) (Feng et al., 2017). These data did not explicitly rule out the possibility that Mcm10 and CST functionally overlap at telomeres, but demonstrated that telomere erosion in *MCM10* mutants was not due to impaired G-overhang generation.

To understand whether Mcm10 deficiency might drive cells into telomere crisis, we propagated six independent *MCM10*$^{+/-}$ populations for >75 PDs. TRF analysis documented that these populations contained telomeres between 2-4 kb in length (Figure 4D). Consistent with these data, the frequency of t-FISH signal free ends remained elevated in *MCM10*$^{+/-}$ cells, but was not increased in comparison to early passage mutants (Figure S2G, 4B). Again, we did not detect changes in telomere fragility (Figure S2G). These observations suggested that short telomere length stabilized in late passage *MCM10*$^{+/-}$ populations. To evaluate this idea, we first confirmed the genotype of each population. Unexpectedly, only three populations carried the heterozygous PCR pattern and three populations had spontaneously reverted the exon 14 mutations. Reversion resulted in two alleles carrying wild type coding sequence. Some cell lines retained the 3' *loxP* site on both alleles, while others lost the *loxP* sites completely (Figure 4E). These results prompted us to conduct additional long-term experiments closely monitoring PDs, telomere length and genotype.

Analysis of these time courses revealed two novel spontaneous reversion events (Figure 4F). Importantly, *MCM10* reversion corresponded with rescued telomere length (Figure 4F), increased Mcm10 levels (Figure 4G), growth rate recovery (Figure 4H) and rescued defects in cell cycle distribution (Figure 4I).

To confirm that reversion events were not the misinterpretation of culture contamination with wild type cells, we marked five independent *MCM10*$^{+/-}$ populations with a puromycin (PURO) resistance gene. Following drug selection the genotype of each population was confirmed as heterozygous and cell lines were propagated and collected at regular time intervals. Each population underwent additional PURO selection twice during the time course (Figure S2H). We found no evidence of reversion in 4/5 populations after ~100 PDs, whereas one population spontaneously reverted (Figure S2I). In this population, telomeres eroded initially but recovered and stabilized following reversion. Taken together, our data demonstrate that the toxic nature of Mcm10 deficiency was actively selected against, as *MCM10*$^{+/-}$ cells spontaneously reverted the locus to restore the *MCM10* coding sequence and rescue mutant phenotypes.

Deficiency of essential replisome proteins Cdc45 or Mcm4 does not cause telomere erosion

The mutant phenotypes in *MCM10*$^{+/-}$ cells led us to ask if HCT116 cells are broadly sensitive to heterozygosity of essential replisome genes. To test this, we constructed *CDC45*$^{+/-}$ and *MCM4*$^{+/-}$ cell lines. These genes encode CMG helicase proteins and contribute to the same processes that require Mcm10 (Baxley and

14

Bielinsky, 2017). $CDC45^{+/-}$ and $MCM4^{+/-}$ cell lines showed reduction in the protein corresponding to the inactivated gene, but no change in Mcm10 levels (Figure S3A). Unexpectedly, Cdc45 levels were significantly reduced in $MCM4^{+/-}$ mutants, suggesting that Mcm4 stabilizes Cdc45 protein. We also confirmed that Cdc45 and Mcm4 levels remained normal in $MCM10^{+/-}$ cell lines (Figure S3B). $CDC45^{+/-}$ and $MCM4^{+/-}$ populations grew slower than wild type cells (Figure S3C), although the growth phenotype was not as severe as in $MCM10^{+/-}$ cells (Figure 1D). The amount of chromatin-bound PCNA-Ub was similar in $CDC45^{+/-}$ and $MCM4^{+/-}$ mutants in comparison to wild type cells, implying that the number of active forks was not reduced, unlike our observations in $MCM10^{+/-}$ cells (Figure S3D, Figure 3E). Finally, TRF analyses revealed that telomere length was stable in $CDC45^{+/-}$ and $MCM4^{+/-}$ mutants (Figure S3E,F). Taken together, these data argue that HCT116 cells are sensitive to inactivation of one $CDC45$ or $MCM4$ allele, but they are significantly more sensitive to $MCM10$ heterozygosity that is associated with a unique telomere maintenance defect.

Mcm10 deficiency limits telomerase activity in HCT116 and RPE-1 cell lines

To understand the relationship between Mcm10 deficiency and telomerase activity *in vivo*, we passaged cells in the presence of the telomerase inhibitor BIBR1532 (Damm et al., 2001). TRF analyses showed that telomere erosion was exacerbated by telomerase inhibition (Figure 5A), suggesting that Mcm10 deficiency limited, but did not abolish telomerase-dependent elongation. Interestingly, the population of $MCM10^{+/-}$ clone #8 was nearly 100% genetically reverted at PD 70, but telomere length had not recovered (Figure 5A). We continued to propagate this population with and without

15

telomerase inhibitor. Without inhibitor, telomeres efficiently lengthened over time (Figure 5B). However, with inhibitor present telomeres remained short (Figure 5B), confirming that telomerase activity was essential for telomere length recovery in reverted *MCM10* cells.

We then examined whether Mcm10-deficient RPE-1 cells also had telomere maintenance defects. TRF analysis showed that *MCM10*$^{+/-}$ telomeres were shorter than normal RPE-1 cells (Figure 5C), but were unexpectedly longer in late passage cells. To investigate this length difference at early and late passage, we monitored telomere length in wild type and *MCM10*$^{+/-}$ cells at regular intervals. This analysis confirmed that telomeres in early passage *MCM10*$^{+/-}$ cells were shorter than wild type (Figure 5D). Surprisingly, we found that telomeres in both cell lines elongated over time (Figure 5D). These data suggested that telomerase activity in hTERT-immortalized RPE-1 cells was robust enough to catalyze telomere extension, regardless of *MCM10* status. Elongation was telomerase dependent, as telomeres in wild type cells passaged with inhibitor did not lengthen over time (Figure 5E). Given that the same dose in HCT116 cells caused progressive telomere erosion (Figure 5A), these data suggested that the *in vivo* telomerase activity is higher in RPE-1 than HCT116 cells. Furthermore, although telomeres in wild type RPE-1 cells were relatively stable in the presence of inhibitor, the identical treatment caused rapid erosion in *MCM10*$^{+/-}$ mutants (Figure 5E). Taken together, these data support the notion that Mcm10 deficiency limited telomerase-dependent telomere elongation.

Telomere analysis in *MCM10*$^{+/-}$ RPE-1 cells suggested that the cells encountered problems at hard-to-replicate genomic loci. To understand whether this defect reduced

16

cell viability, we used flow cytometry to analyze cells co-stained with PI and annexin V and found a significant increase in late apoptotic and dead $MCM10^{+/-}$ cells (Figure S4A,B). Furthermore, we measured β-gal activity to understand whether $MCM10^{+/-}$ RPE-1 cells activated senescence pathways, but did not detect an increase in comparison to wild type cells (Figure S4C), consistent with the fact that telomeres did not erode without telomerase inhibition (Figure 5D,E). Taken together, our analyses suggested that the $MCM10^{+/-}$ RPE-1 population growth defect (Figure 1E) was caused by cell death following impaired replication of challenging loci, but not global changes in DNA synthesis or cell cycle disruption (Figure 2G-K). These data support the idea that cancer cells (*e.g.*, HCT116) are more reliant on robust Mcm10 expression than non-transformed cells (*e.g.*, RPE-1).

Super-telomerase rescues telomere length but not the inherent replication defect in heterozygous HCT116 *MCM10* mutant cells

　　　Telomerase activity was evidently high enough in RPE-1, but not HCT116 cells to extend telomeres. To test whether increased telomerase activity could overcome the limiting effect of Mcm10 deficiency in HCT116 cells, we transiently overexpressed *hTERT* and a mutant of the telomerase RNA component *hTR*, *TSQ1* (tolerated sequence 1). *TSQ1* expression causes incorporation of mutant CCGCAA repeats and allows detection specifically of nascent telomere repeats (Diolaiti et al., 2013). We did not find any difference in the ability of excess telomerase to extend telomeres in wild type or $MCM10^{+/-}$ cells (Figure S5A). This led us to hypothesize that stable telomerase overexpression could rescue telomere erosion and alleviate $MCM10^{+/-}$ mutant

17

phenotypes. To test this idea, we generated stable cell lines that overexpressed *hTERT* and *hTR* – so-called 'Super-telomerase' (ST) (Cristofari and Lingner, 2006). Most ST cell lines showed significantly longer telomeres (>12 kb) than observed in normal HCT116 cells (~4-6 kb; Figure S5B). ST cell lines with significantly extended telomeres and similar telomerase activities (Figure S5C) were utilized for further experiments. ST expression in $MCM10^{+/-}$ cell lines did not increase steady-state Mcm10 protein levels (Figure S5D) nor rescue the diminished proliferation rate (Figure S5E). In fact, the excessive telomere length slightly decreased clonogenic survival (Figure S5F). Overall, these data demonstrate that ST expression rescued telomere length without promoting proliferation or viability.

The ST cells allowed us to perform telomeric replication assays similar to those used in models with long telomeres (Sfeir et al., 2009). We utilized a DNA combing specifically analyze telomere and sub-telomere replication (Figure 6A). In comparison to wild type ST cells, $MCM10^{+/-}$ ST mutants showed an increase in unreplicated telomeres (Figure 6B). Moreover, telomeres in $MCM10^{+/-}$ ST mutants were more often partially replicated, which is consistent with – but does not prove – increased fork stalling (Figure 6C). Next, we tested whether $MCM10^{+/-}$ ST mutants generated C-circles; extra-chromosomal single-stranded DNAs produced by telomere replication stress (Henson et al., 2009, O'Sullivan et al., 2014, Rivera et al., 2017). Although ST cell lines showed increased C-circle signals in comparison to normal HCT116 cells, no significant change was observed in $MCM10^{+/-}$ ST cells (Figure S6A). Thus, we used 2-dimensional (2D) gel analyses to detect DNA intermediates associated with telomeric replication stress. A low intensity t-circle arc was observed in all ST cell lines (Figure 6D). Strikingly, however,

18

MCM10^{+/-} ST cells significantly accumulated t-complex DNA, which is comprised of branched DNA structures containing internal ssDNA gaps (Figure 6D) (Nabetani and Ishikawa, 2009). Treatment of wild type HCT116 ST cells with HU generated t-complex DNA (Figure 6E), suggesting that these structures are products of replication stress. To further evaluate the nature of t-complex DNA, samples were treated with S1-nuclease to degrade ssDNA. Wild type ST samples were unchanged after S1-nuclease digestion, whereas a significant reduction in t-complex signal occurred in S1-digested *MCM10*^{+/-} ST samples (Figure 6F). These data argued that the accumulated t-complexes in *MCM10* mutants were enriched for ssDNA gaps. Furthermore, the severity of chronic Mcm10 deficiency in ST cells also stimulated spontaneous reversion that rescued the accumulation of t-complex DNA and the proliferation defect (Figure S6B,C). The generation of t-complexes is poorly understood, but their characterization was consistent with regressed forks and/or recombination intermediates (Nabetani and Ishikawa, 2009). To delineate between these possibilities, we measured the frequency of telomere sister chromatid exchanges (t-SCEs) that are produced by homologous recombination. *MCM10*^{+/-} ST cells showed a similar frequency of t-SCEs as wild type ST cells (Figure 6G), suggesting the stalled telomeric replication forks caused by Mcm10 deficiency were not rescued by recombination.

Loss of Mus81 exacerbates viability and telomere maintenance defects in Mcm10-deficient cells

One mechanism to resolve fork stalling is the recruitment of structure-specific endonucleases (SSEs) to cleave replication intermediates and stimulate restart. A major

player in this pathway is the Mus81 endonuclease, which functions in complex with Eme1 or Eme2, as well as the Slx1-Slx4/Mus81-Eme1/XPF-Ercc1 (SMX) DNA-repair trinuclease (Falquet and Rass, 2019). We hypothesized that *MCM10* mutants relied on SSE-dependent fork cleavage to overcome fork stalling. To test this, we generated *MCM10$^{+/-}$:MUS81$^{-/-}$* double mutants. Wild type and *MCM10$^{+/-}$* cells expressed equivalent Mus81 protein levels, whereas Mus81 was not detectable in *MUS81$^{-/-}$* mutants (Figure 7A). Importantly, Mcm10 expression was not altered following *MUS81* knockout (Figure 7A). *MUS81$^{-/-}$* cells showed a growth defect, although not as severe as seen in *MCM10$^{+/-}$* mutants (Figure 7B). Furthermore, this defect was significantly worse in the double mutants, which proliferated ~2-fold slower than *MCM10$^{+/-}$* single mutants (Figure 7B). Comparison of clonogenic survival yielded similar results, wherein *MUS81$^{-/-}$* cells showed a defect that was less severe than *MCM10$^{+/-}$* mutants and *MCM10$^{+/-}$:MUS81$^{-/-}$* cells showed a stronger phenotype than either single mutant (Figure 7C). Increased apoptosis or cell death was not detected in *MUS81* single mutants (Figure 7D). However, we measured a significant increase in double mutant cell death (Figure 7D). Next, we utilized TRF analysis to examine alterations in telomere maintenance. *MUS81* knockout caused telomere erosion, and loss of Mus81 in *MCM10$^{+/-}$* cells caused more significant erosion than in either single mutant. Furthermore, we found elevated β-gal signal in *MUS81* knockouts, with the highest levels detected in the double mutants (Figure 7F). Taken together, our data clearly demonstrate a requirement for Mus81 in promoting cell proliferation and viability in Mcm10-deficient cells, likely through stimulating replication restart in hard-to-replicate regions, including telomeres (Figure 7G).

20

21

Discussion

Robust Mcm10 expression is essential to maintain genome stability

Reduced Mcm10 expression in HCT116 mutants severely inhibited faithful genome duplication. The primary alterations to global replication in these cells was 1) reduced origin firing (Figure 3C), and 2) modestly increased fork speed (Figure 3D). The latter is likely a mechanism to compensate for the initiation defect, as the rate of origin firing and fork speed are inversely regulated in eukaryotes (Rodriguez-Acebes et al., 2018, Zhong et al., 2013). Previous combing analyses following Mcm10 knockdown reported decreased IODs and reduced or unaltered fork speed (Fatoba et al., 2013, Miotto et al., 2014). It is important to note that these studies reflect the response to rapid, nearly complete Mcm10 depletion, whereas our analyses described phenotypes triggered by stable Mcm10 reduction to ~50%. Remarkably, the chronic stress in $MCM10^{+/-}$ HCT116 cells was severe enough to stimulate spontaneous reversion of the exon 14 mutation and rescue of $MCM10$ mutant phenotypes (Figure 4F-I). Although we did not detect changes in global fork stability (Figure 3E), the 80% overlap of chromosomal aberrations with CFSs (Table 1) and impaired telomere replication (Figure 6B,C) argue that fork stalling occurred frequently at these specific loci. Unlike in HCT116 cells, we did not detect a DNA synthesis defect in $MCM10^{+/-}$ RPE-1 cells (Figure 2K), despite a significantly reduced proliferation rate (Figure 1E). We propose that this phenotype was caused by increased cell death (Figure S4B) due to impaired replication at hard-to-replicate loci, similar to HCT116 mutants, as evidenced by telomere maintenance defects observed in both cell types (Figure 4,5). Taken together,

our data demonstrate that robust Mcm10 expression is critical for duplication of genomic loci that are prone to replication stress.

There is growing consensus that Mcm10 promotes replisome stability (Baxley and Bielinsky, 2017, Chadha et al., 2016, Looke et al., 2017), although the mechanism has remained unclear. A recent study demonstrated that yeast Mcm10 is important for bypassing lagging strand blocks (Langston et al., 2017), suggesting that Mcm10 is critical when the replisome encounters barriers to CMG translocation. Consistent with this idea, *MCM10*$^{+/-}$ cells were not more sensitive to drugs that inhibited polymerase progression, but were sensitive to MMC, which induces inter-strand crosslinks that present a strong helicase barrier (Figure 3G; Figure S1C). However, the lack of sensitivity to cisplatin or etoposide (Figure S1C), which would also introduce CMG-blocking lesions, implies a distinct requirement for Mcm10 in protecting MMC-induced stalled forks. Recently, yeast Mcm10 was shown to prevent translocase-mediated fork regression (Mayle et al., 2019). If human Mcm10 functions similarly, it might not only prevent stalling but also inhibit regression to promote restart. In support of this model, we argue that t-complex DNA in *MCM10* mutants was produced by regression of stalled telomeric replication forks (Figure 7G). Furthermore, yeast Mcm10 was required for fork restart *in vitro* (Wasserman et al., 2019) and thus, human Mcm10 may also be involved in many aspects of the replication stress response at active forks. Without sufficient Mcm10, cells must rely on alternative pathways to restart DNA replication. Our data implicate SSEs, including the Mus81 protein, in processing these forks to rescue DNA synthesis and promote *MCM10*$^{+/-}$ cell viability (Figure 7G).

Mcm10 deficiency limits telomerase-dependent telomere length maintenance

We were surprised to discover that reduced Mcm10 expression impaired telomere extension by telomerase. This effect was not due to decreased enzymatic telomerase function, as *in vitro* activity was unaltered in the mutants (Figure 4C). Moreover, the limiting effect of Mcm10 deficiency was overcome with sufficiently high telomerase expression (Figure S5B), although the underlying replication defects persisted. We propose that fork stalling and arrest in *MCM10* mutants prevented the replisome from reaching chromosome ends. This could cause telomere erosion in several ways. First, telomere replication defects might delay the generation of chromosome ends suitable for telomerase extension. Because telomere replication and telomerase-dependent synthesis primarily later in S-phase (Arnoult et al., 2010, Piqueret-Stephan et al., 2016, Tomlinson et al., 2006), the replication defect could delay telomere maturation and shorten the cell cycle window when telomerase can act. Second, because reversed replication forks are a substrate for telomerase (Margalef et al., 2018), increased fork stalling and regression could alter telomerase recruitment or activity. Third, terminal fork arrest in the proximal telomere requiring nucleolytic cleavage to form a functional chromosome end could result in the loss of a significant portion of the distal telomere.

We have demonstrated an unexpected link between Mcm10 deficiency and telomere maintenance in telomerase-positive cell lines. However, a role for Mcm10 in ALT telomere maintenance has not been investigated. Recent studies have outlined distinct differences in telomere replication between telomerase-positive and ALT cancer cells (Dilley et al., 2016, Sobinoff et al., 2017, Zhang et al., 2019). For example, ALT

24

cells synthesize telomeres in promyelocytic leukemia (PML) bodies and accumulate high levels of t- and C-circle DNA, unlike telomerase-positive cells (Dilley et al., 2016, Sobinoff et al., 2017). In agreement, we detected very low levels of t- or C-circle DNAs in HCT116 ST cells (Figure 6D,F; Figure S6A,B). However, the presence of these DNA species suggested that they are not fundamentally exclusive to ALT cells, which is supported by their detection in non-ALT cell lines previously (O'Sullivan et al., 2014, Rivera et al., 2017). In $MCM10^{+/-}$ ST cells we observed a significant increase in t-complex DNA (Figure 6D,F; Figure S6B). The source of this high-molecular weight DNA species is enigmatic, but what is clear is that the majority contains branched structures with significant regions of ssDNA (Nabetani and Ishikawa, 2009). Our data suggest that t-complexes are intermediates of stalled fork processing, but not products of recombination between sister telomeres (Figure 6A-G). Although ALT cells rely on break-induced replication to maintain telomere length, telomere replication presumably begins with synthesis by the canonical replisome. Based on these observations, we propose that t-complexes are the result of fork remodeling, whereas t- and C-circles are more specifically products of break-induced telomere replication.

Regulation of *MCM10* expression in the context of human disease

Previous studies of human Mcm10 relied on overexpression of epitope-tagged constructs and/or knockdown to significantly reduce Mcm10 levels over few cell divisions (Baxley and Bielinsky, 2017). Our work examined the consequences of chronic Mcm10 deficiency over many PDs. We demonstrated that *MCM10* is haploinsufficient in HCT116 and RPE-1 cell lines. Our analyses of HCT116 mutants also demonstrated that

25

CDC45 and *MCM4* are haploinsufficient. Because HCT116 is a rapidly proliferating cancer cell line, it is likely that additional replication genes are haploinsufficient, with the phenotypic severity dependent on genetic background and expression levels of other factors. During oncogenic transformation, cells overexpress replication factors to drive proliferation (Das et al., 2013, Garcia-Aragoncillo et al., 2008, Wu et al., 2012). Consistent with this idea, origin licensing and DNA synthesis were significantly higher in HCT116 cancer cells than in non-transformed RPE-1 cells (Figure 2L,M). Thus, the increased demand for Mcm10 in HCT116 cells rendered them more sensitive to *MCM10* depletion. Overall, we propose that the proliferation and viability defects observed in Mcm10-deficient cells stem from incomplete replication due to reduced origin firing and fork stalling that leads to progressive genome instability. The observation that transformed cells are more dependent on robust *MCM10* expression suggests that compounds that target Mcm10 (Paulson et al., 2019) might be useful to preferentially sensitize cancer cells to treatment with common chemotherapeutic drugs.

Deletion of *MCM10* exon 14 was used to model a NKD-associated nonsense mutation (c.C1744T, p.R582X) (Mace et al., bioRxiv doi: 10.1101/825554, 2019). Our studies of *MCM10*$^{+/-}$ cells argue that increased genome instability contributed to NKD in this patient, similar to the cellular phenotypes caused by NKD associated mutations in replication factors *MCM4* and *GINS1* (Cottineau et al., 2017, Gineau et al., 2012, Hughes et al., 2012). Notably, our data suggest that *MCM10*-associated NKD was not solely attributable to haploinsufficiency. The patient inherited the missense and nonsense mutations from the mother and father, respectively. Because *MCM10*-associated pathology has not been described in either parent, we presume that both

26

mutations were required to cause the patient's clinical phenotype. This interpretation is consistent with the relatively modest phenotypes observed in our non-transformed RPE-1 *MCM10* mutants, and further supported by analysis of RPE-1 cells carrying either the missense or nonsense mutations, which independently caused proliferation defects (Mace et al., bioRxiv doi: 10.1101/825554, 2019).

The unexpected effect of Mcm10 deficiency on telomere maintenance suggests that premature replicative senescence could be inhibiting robust NK cell maturation. It is currently unknown whether the NKD-associated *MCM4* or *GINS1* mutations affect telomere maintenance. Notably, we did not observe telomere erosion in heterozygous *MCM4* or *CDC45* mutants, suggesting that telomere maintenance defects are not *per se* inherent to replisome mutations. However, a NKD patient was identified carrying a mutation in *RTEL1* (*regulator of telomere length 1*) (Hanna et al., 2015), an essential DNA helicase required for replication and maintenance of mammalian telomeres (Ding et al., 2004, Uringa et al., 2012). Interestingly, Mcm10 was identified as an RTEL1-interacting protein in mass spectrometry analyses of murine cells (Vannier et al., 2013), arguing that a shared requirement for telomere replication may underlie NKD observed in these patients. Finally, limited evidence suggests that NK cells have shorter telomeres than T- and B-cells, although they arise from a common progenitor, and that telomerase activity decreases as NK cells differentiate (Fali et al., 2019, Ouyang et al., 2007, Romagnani et al., 2007). These phenotypes may explain why the NK cell lineage is particularly sensitive to defects in telomere replication. Therefore, future investigations of the link between telomere maintenance, NK cell development and the eukaryotic replisome could provide valuable insights regarding NKD.

27

28

Acknowledgments

Author Contributions

Conceptualization, A.K.B. and R.M.B.; Methodology, A.K.B., R.M.B., J.P.M., J.G.C.; Formal Analysis, A.K.B., R.M.B., J.P.M.; Investigation, R.M.B., M.M.S., M.K.O., J.P.M., L.W., W.L., C.B.R., D.B., J.H., A.H.; Writing – Original Draft, R.M.B. and A.K.B.; Writing – Review & Editing, R.M.B., A.K.B., J.G.C., E.A.H., E.M.M., J.S.O. Visualization, R.M.B., J.P.M.; Supervision, A.K.B., and J.G.C,; Project Administration, A.K.B. and R.M.B.; Funding Acquisition, A.K.B. and J.G.C.

Declaration of Interests

The authors declare no competing interests.

Figure Titles and Legends

Figure 1. *MCM10* heterozygous HCT116 and RPE-1 cell lines have reduced Mcm10 expression and impaired proliferation.

A) Schematic of the human *MCM10* indicating exons targeted using CRISPR-Cas9 (exon 3) or rAAV (exon14) to generate *MCM10*$^{+/-}$ cell lines.

B) *MCM10*$^{+/-}$ exon 14 genotyping of alleles carrying a *loxP* site 3' of exon 14 (upper band) or a *loxP* scar (lower band), in comparison to the wild type locus (middle band). A faint non-specific band is noted (asterisk).

C) Western blot for Mcm10 with GAPDH (left) or Tubulin (right) as a loading control. Quantification of Mcm10 levels normalized to loading control, relative to wild type is indicated.

D-E) Average proliferation rate in *MCM10*$^{+/-}$ cells normalized to wild type. For each cell line n=6 wells across three biological replicates.

F) Comparison of clonogenic survival of HCT116 wild type (top) and *MCM10*$^{+/-}$ cells (middle/bottom). Cells plated per well are noted.

G) Percentage clonogenic survival in HCT116 wild type (blue) and *MCM10*$^{+/-}$ cells (red), n = 15 wells across ten biological replicates. Error indicated in **D, E** and **G** as standard deviation and significance was calculated using students *t-test* with *>.05; **>.01, ***>.001.

Figure 2. Mcm10 deficiency causes significant cell cycle and DNA synthesis defects in HCT116, but not RPE-1 cell lines.

A) Cell cycle distribution of HCT116 wild type and *MCM10*^{+/-} cells. Percentage of each population in G1- (green), S- (purple) or G2/M-phase (gray) is shown.

B) Cell cycle distribution of HCT116 wild type and *MCM10*^{+/-} cell lines from three biological replicates. Percentage of each population in G1- (green), S- (purple) and G2/M-phase (gray) is shown.

C) Schematic of flow cytometry analysis. Cell-cycle phase is defined by DNA content, EdU incorporation and chromatin loaded MCM2.

D) Analytical flow cytometry plots for HCT116 wild type and *MCM10*^{+/-} cells. G1-phase/MCM positive cells (blue), S-phase/MCM positive cells (orange) and G1- or G2/M-phase/MCM negative cells (gray) are indicated.

E) Comparison of origin licensing (left) and quantification of G1 loaded MCM2 (n=3) in HCT116 wild type (gray) and *MCM10*^{+/-} cells (blue/green).

F) Comparison of S-phase DNA synthesis (left) and mean EdU intensity (n=3) in HCT116 wild type (gray) and *MCM10*^{+/-} cells (red/orange).

G) Cell cycle distribution of RPE-1 wild type and *MCM10*^{+/-} cells. Percentage of each population in G1- (green), S- (purple) and G2/M-phase (gray) is shown.

H) Cell cycle distribution of RPE-1 wild type and *MCM10*^{+/-} cells from three biological replicates. Percentage of each population in G1- (green), S- (purple) and G2/M-phase (gray) is shown.

31

I) Flow cytometry plots for RPE-1 wild type and *MCM10*$^{+/-}$ cells. G1-phase/MCM positive cells (blue), S-phase/MCM positive cells (orange) and G1- or G2/M-phase/MCM negative cells (gray) are indicated.

J) Comparison of origin licensing (left) and G1 loaded MCM2 (n=3) in RPE-1 wild type (gray) and *MCM10*$^{+/-}$ cells (blue).

K) Comparison of S-phase DNA synthesis (left) and mean EdU intensity (n=3) in RPE-1 wild type (gray) and *MCM10*$^{+/-}$ cell lines (red).

L) G1 loaded Mcm2 (n=3) in wild type HCT116 (gray) and RPE-1 (blue) cells.

M) Mean EdU intensity (n=3) in wild type HCT116 (red) and RPE-1 (gray) cells. Error bars in **B, E, F, H, J, K, L** and **M** indicate standard deviation and significance was calculated using students *t-test* with *>.05; **>.01, ***>.001.

Figure 3. *MCM10*$^{+/-}$ **HCT116 cells display DNA replication defects and increased cell death.**

A) Example DNA fibers used for DNA combing analyses. Scale bar is 5 µm.

B) Inter-origin distance (IOD) quantification from three technical replicates across two biological replicates in wild type (blue) and *MCM10*$^{+/-}$ cells (red). Average IOD and number (n) quantified is listed.

C) Fork speed from three technical replicates across two biological replicates in wild type (blue) and *MCM10*$^{+/-}$ cells (red). Average fork speed (kb/minute) and number (n) quantified is listed.

D) Fork stability from three technical replicates across two biological replicates in wild type (blue) and *MCM10*$^{+/-}$ cells (red). Average fork stability and number (n) quantified is

listed. Statistical significance for **B-D** was calculated using Mann-Whitney Ranked Sum Test with *>.05; **>.01, ***>.001.

E) Chromatin associated PCNA, PCNA-Ub and phospho-RPA32, with and without 40J UV treatment. Quantification of PCNA-Ub levels normalized to unmodified PCNA, relative to the first lane wild type sample is indicated.

F) Percentage of each population represented by early apoptotic, late apoptotic or dead cells, n=4 replicates across two biological replicates.

G) Clonogenic survival in HCT116 wild type (blue) and clonal $MCM10^{+/-}$ cells (red) treated with UV (top), HU (middle) or MMC (bottom), n>3 replicate wells across at least two biological replicates for all data points. Error bars in **F** and **G** indicate standard deviation and significance was calculated using students *t-test* with *>.05; **>.01, ***>.001.

Figure 4. Mcm10 deficiency causes telomere erosion that is rescued following spontaneous reversion of the *MCM10* mutant locus.

A) Telomere restriction fragment (TRF) length analysis of HCT116 wild type (left) and $MCM10^{+/-}$ cells (right). Estimated PDs is indicated. Yellow dots indicate the location of peak intensity.

B) Signal free-ends (left) and fragile telomeres (right) in HCT116 wild type (blue) and $MCM10^{+/-}$ cells (red). Statistical significance was calculated using students *t-test* with ***<.001; n>143 metaphases per cell line. Scale bars are 1 μm.

C) TRAP assay from HCT116 wild type (left) and $MCM10^{+/-}$ cells (right). The internal PCR control at 36bp and telomerase above 50bp are noted.

D) TRF analysis of HCT116 wild type (left) and independent late passage $MCM10^{+/-}$ cell populations from two parental $MCM10^{+/-}$ cell lines (right). Yellow dots indicate the location of peak intensity.

E) $MCM10^{+/-}$ exon 14 genotyping PCR in late passage $MCM10^{+/-}$ populations showing alleles that have one *loxP* site 3' of exon 14 (upper band) or a *loxP* scar (lower band), as well as exon 14 reverted alleles that have retained or lost the 3' *loxP* site. A faint non-specific band can also be detected (asterisk).

F) TRF analysis in HCT116 wild type and $MCM10^{+/-}$ cells (top). PDs for each population are shown. Yellow dots indicate the location of peak intensity. Genotyping PCR for each TRF sample is shown (bottom).

G) Western blot analyses for Mcm10 with Tubulin as a loading control. Quantification of Mcm10 levels normalized to loading control, relative to the first lane wild type sample is indicated. PDs for each cell line are noted.

H) Proliferation rate in HCT116 wild type, $MCM10^{+/-}$ and reverted cells normalized to early passage wild type cells, for each cell line n=6 replicate wells across two biological replicates.

I) Cell cycle distribution of HCT116 wild type, $MCM10^{+/-}$ and reverted cell lines, n=4 across two biological replicates. Percentage of each population in G1- (green), S- (purple) and G2/M-phase (gray) is shown. Error bars in **H** and **I** indicate standard deviation and significance was calculated using students *t-test* with *>.05; **>.01, ***>.001.

Figure 5. Mcm10 levels are limiting for telomerase-dependent telomere elongation.

A) TRF analysis in HCT116 wild type and *MCM10*$^{+/-}$ cells (top) in the presence of 10μM telomerase inhibitor BIBR1532. PDs for each population are shown. Yellow dots indicate the location of peak intensity. Genotyping PCR for each time point is shown (bottom).

B) TRF analyses in *MCM10*$^{+/-}$ clone #8 reverted cells in the presence or absence of telomerase inhibitor. PDs for each population are indicated. Yellow dots indicate the location of peak intensity.

C) TRF analysis in *MCM10*$^{+/-}$ RPE-1 cell lines. Estimated PDs are indicated. Yellow dots indicate the location of peak intensity.

D) TRF analysis in RPE-1 wild type and *MCM10*$^{+/-}$ clone #20. PDs for each cell line are noted. Yellow dots indicate the location of peak intensity.

E) TRF analysis RPE-1 wild type and *MCM10*$^{+/-}$ clone #20 in the presence of telomerase inhibitor. PDs for each cell line are noted. Yellow dots indicate the location of peak intensity.

Figure 6. Telomeric replication stress is increased in ST *MCM10*$^{+/-}$ HCT116 cells.

A) Telomere combing images with telomeric DNA (green), nascent DNA (red) and merged images with examples of unreplicated telomeres (left), partially replicated (middle) and completely replicated telomeres (right). Telomeric and sub-telomeric regions are indicated. Scale bars are 3 μm.

B) Average percentage of unreplicated telomeres in wild type (blue) and *MCM10*$^{+/-}$ cell lines (red) ST cell lines, n= total number of telomeres quantified including two or more replicate experiments.

C) Average percentage of completely replicated (yellow) versus partially/stalled telomeres (green) in ST cell lines, n= total number of replicated telomeres quantified including two or more replicate experiments. Error bars in **B** and **C** indicate standard deviation and significance was calculated using students *t-test* with *>.05; **>.01, ***>.001.

D) (Left) Cartoon of t-complex DNA as depicted previously (Nabetani and Ishikawa, 2009). (Middle) Diagram of double-stranded telomere restriction fragment (ds-TRF), telomere circle (t-circle) and telomere complex (t-complex) DNA species from 2D gel electrophoresis. (Right) Comparison of 2D gels from ST cell lines.

E) Comparison of DNA species from 2D gel electrophoresis in HCT116 wild type ST cells with (bottom) and without (top) 4-day HU treatment.

F) Comparison of DNA species from 2D gels in HCT116 wild type and *MCM10*^{+/-} ST cell lines with (bottom) and without (top) S1 nuclease digestion.

G) (Left) Image of t-SCE staining in ST cell lines. Examples of a t-SCE event and chromosomes without t-SCE are highlighted. (Right) Percentage t-SCE per chromosome ends in ST cell lines. Bars represent median percentage t-SCE per chromosome ends; n=>14 metaphases for each cell line. Significance was calculated using students *t-test* with *>.05; **>.01, ***>.001. Scale bar is 10 μm.

Figure 7. Loss of Mus81 increases the severity of proliferation, viability and telomere length defects in *MCM10*^{+/-} cell lines.

A) Western blot analyses for Mus81 and Mcm10 with GAPDH (left) as a loading control. Quantification of Mcm10 levels normalized to tubulin loading control, relative to the first lane wild type sample is indicated.

B) Proliferation rate in HCT116 wild type, $MUS81^{-/-}$, $MCM10^{+/-}$ and double mutant cell lines normalized to HCT116 wild type, n=6 replicate wells across three biological replicates.

C) Comparison of clonogenic survival of HCT116 wild type, $MUS81^{-/-}$, $MCM10^{+/-}$ and double mutant cell lines.

D) Average percentage of each population represented by early apoptotic, late apoptotic or dead cells in HCT116 wild-type, $MUS81^{-/-}$, $MCM10^{+/-}$ and double mutant cell lines, n=2 replicates for HCT116 wild type and $MCM10^{+/-}$ single mutants; n=4 replicates across two biological replicates for all $MUS81^{-/-}$ cell lines.

E) TRF analysis of early passage HCT116 wild type, $MUS81^{-/-}$, $MCM10^{+/-}$ and double mutant cell lines. Yellow dots indicate the location of peak intensity.

F) β-gal activity expressed as arbitrary fluorescence units normalized to total protein for $MUS81^{-/-}$ (black) and $MUS81^{-/-}$, $MCM10^{+/-}$ mutant cell lines (gray). Average levels for HCT116 wild type and $MCM10^{+/-}$ cell lines from Figure S2D are indicated with dashed lines, n=3 replicate wells for all data points. Error bars in **B, D** and **F** indicate standard deviation and significance was calculated using students t-$test$ with *>.05; **>.01, ***>.001.

G) Model of telomere replication defects in Mcm10-deficient cells. Fork stalling occurs as the active replisome moves through the telomere. Stalled forks may restart efficiently or require regression and/or processing to stimulate restart. Complete replication

37

generates chromosome ends accessible for telomerase-dependent telomere synthesis. When Mcm10 is deficient, the frequency of fork stalling and regression increases significantly. Nucleolytic processing by Mus81 may stimulate replication restart or might remove the distal telomere completely to generate a chromosome end that can be a substrate for telomerase. Fork collapse and degradation is increased in Mcm10 mutants, which along with regressed forks constitute t-complex DNA. Overexpression of Super-telomerase can overcome the limiting effect of Mcm10 deficiency to efficiently elongate telomeres.

STAR Methods

LEAD CONTACT AND MATERIAL AVAILABILITY

Further information and requests for resources and reagents should be directed to and will be fulfilled by the Lead Contact, Anja-Katrin Bielinsky (bieli003@umn.edu).

EXPERIMENTAL MODEL AND SUBJECT DETAILS

Cell Lines

HCT116 cells (RRID:CVCL_0291) were grown in McCoy's 5A medium (Corning 10-050-CV) supplemented with 10% FBS (Sigma F4135), 1% Pen Strep (Gibco 15140) and 1% L-Glutamine (Gibco 205030). hTERT RPE-1 (referred to as RPE-1; RRID:CVCL_4388) cells were grown in DMEM/F12 medium (Gibco 11320) supplemented with 10% FBS and 1% Pen Strep. Cells were cultured at 37˚C and 5% CO_2. Cell lines used in this study were authenticated using several methods including: morphology check by microscope, growth curve analyses, mycoplasma detection, PCR and Sanger

38

sequencing, and high-quality G-band karyotype analyses. Karyotype analyses were performed by the Cancer Genomics Shared Resource (CGSR) as part of the MCC Cytogenomics Shared Service and the University of Minnesota Genomics Center (UMGC).

METHOD DETAILS

Cell Line Generation using rAAV

HCT116 *MCM10*$^{+/-}$ (exon 14) cell lines were generated using rAAV (recombinant adeno-associated virus)-mediated gene targeting (Kohli et al., 2004). The conditional vector pAAV-MCM10-cond was constructed using Golden Gate cloning and designed as described previously (Kohli et al., 2004, Thompson et al., 2017). The MCM10-cond rAAV was generated by co-transfection of pAAV-MCM10-cond, pAAV-RC (Kohli et al., 2004), and pHelper (Kohli et al., 2004) into HEK293 cells using Lipofectamine LTX (Invitrogen 15338030) following standard protocols (Kohli et al., 2004). The first round of targeting replaced *MCM10* exon 14 with a wild type allele with a downstream neomycin (G418) selection cassette flanked by *loxP* sites ("floxed"). Targeted clones were selected using 0.5 mg/ml G418 (Geneticin G5005). Resistant clones were screened by PCR using primers within the neomycin cassette and outside the rAAV homology arms to confirm locus-specific targeting, and Cre (cyclization recombinase) transiently expressed from an adenoviral vector (AdCre; Vector Biolabs #1045) was then used to remove the neomycin selection cassette as described (Kohli et al., 2004, Thompson et al., 2017). The second round of *MCM10* gene targeting used the same rAAV vector and replaced the wild type allele with a floxed allele and a downstream floxed neomycin

39

selection cassette. G418-resistant clones were screened by PCR to confirm locus-specific targeting. AdCre recombinase was then used to remove the neomycin selection cassette and resulted in the generation of heterozygous *MCM10* clones. The *MCM10* exon 14 genotype was subsequently screened and confirmed using primers flanking the exon.

Cell Line Generation using CRISPR/Cas9

HCT116 and RPE-1 *MCM10*$^{+/-}$ (exon 3), HCT116 *CDC45*$^{+/-}$ exon 3 and HCT116 *MCM4*$^{+/-}$ exon 2 cell lines were generated using CRISPR/Cas9 (clustered regularly interspaced short palindromic repeats/CRISPR associated 9) gene targeting. Guide RNAs (gRNA) were designed such that DNA cleavage would disrupt endogenous restriction enzyme recognition sites. The gRNAs were cloned into a CRISPR/Cas9 plasmid hSpCas9(BB)-2A-GFP (PX458; RRID:Addgene_48138) as described previously (Ran et al., 2013). Cells were transfected with CRISPR/Cas9 plasmid containing gRNA using the Neon Transfection System (Invitrogen MPK5000) following standard protocols. Two days post-transfection GFP-positive cells were collected by flow cytometry (University of Minnesota Flow Cytometry Resource (UFCR)). Subcloned cells were screened for correct targeting by PCR amplification and restriction enzyme digestion (*MCM10* exon 3, Hpy199III (NEB R0622); *CDC45* exon 3, PflMI (NEB R0509), XcmI (NEB R0533) or AlwNI (NEB R0514); *MCM4* exon 2, BglI (NEB R0143). Specific mutations were identified by PCR and Illumina sequencing or PCR, DNA sequencing and TIDE (Tracking of Indels by Decomposition) analyses (Brinkman et al., 2014).

To generate HCT116 *MUS81*$^{-/-}$ exon 2 mutant cell lines, each parental line was transfected with 1 µL of 100 µM sgRNA (Synthego Corporation, Redwood City, CA, US) and 1 µg Cas9 mRNA (TriLink #L-7206) using the Neon Transfection System following standard protocols. Three days post-transfection cells were subcloned. Subclones were screened for correct targeting by PCR amplification, DNA sequencing and TIDE analyses.

Cell Line Generation using plasmid transfection

To generate HCT116 cells lines expressing Super-Telomerase (Cristofari and Lingner, 2006), pBABEpuroUThTERT+U3-hTR-500 (Wong and Collins, 2006) was purchased from Addgene (RRID:Addgene_27665), linearized with restriction enzyme ScaI (NEB R3122) and transfected into wild type or mutant HCT116 cell lines following standard Lipofectamine 3000 protocols (Invitrogen L3000). Stable cell lines were generated using puromycin selection (1 µg/ml; Sigma P7255) followed by subcloning. Subclones were screened for Super-Telomerase activity by TRF analysis and TRAP assay (details below).

Cell Proliferation

Cells were plated at 50,000 cells per well (hTERT RPE-1) or 100,000-125,000 cells per well (HCT116) in 6-well plates. Cell counts were performed 3-days after seeding using Trypan Blue (Invitrogen T10282) on Countess slides (Invitrogen C10283) using a Countess automated cell counter (Invitrogen C20181).

41

Protein Extraction, Chromatin Fractionation and Western Blotting

For preparation of whole cell extracts, cells were lysed in RIPA (50 mM Tris-HCl, pH 8.0, 150 mM NaCl, 10 mM NaF, 1% NP-40, 0.1% SDS, 0.4 mM EDTA, 0.5% sodium deoxycholate, 10% glycerol) buffer for 10 min and then centrifuged at 16,000 g for 10 min. Cleared lysates were collected, mixed with SDS loading buffer and boiled before fractionation by SDS-PAGE and analyses by western blot. Chromatin fractions were isolated as previously described (Becker et al., 2018, Motegi et al., 2008). Briefly, extracts were prepared by lysis in Buffer A (10 mM HEPES pH 7.9, 10 mM KCl, 1.5 mM MgCl$_2$, 0.34 M sucrose, 10% glycerol, 0.1% triton X-100 and protease inhibitors). Insoluble nuclear proteins were isolated by centrifugation and chromatin bound proteins were subsequently released by sonication. Remaining insoluble factors were cleared by centrifugation before fractionation by SDS-PAGE and western blot analyses. Primary antibodies were incubated in 5% BLOT-QuickBlocker (G-Biosciences 786-011) as follows: rabbit anti-Mcm10 (Bethyl, A300-131A; 1:500; RRID:AB_2142119), rabbit anti-Mcm10 (Novus, H00055388-D01P, 1:500; RRID:AB_11047378), mouse anti Cdc45 (Santa Cruz, G12, SC55568; 1:500; RRID:AB_831145), mouse anti-Mcm4 (Santa Cruz, G7, SC28317; 1:500; RRID:AB_627916), mouse anti-Mus81 (Abcam, ab14387; 1:500; RRID:AB_301167), mouse anti-PCNA (Abcam, Ab29; 1:3,000; RRID:AB_303394), rabbit anti-RPA32 (S4/8) (Bethyl, A300-245A; 1:2000; RRID:AB_210547), mouse anti-GAPDH (GeneTex GTX627408; 1:5,000; RRID:AB_11174761), mouse anti-α-Tubulin (Millipore, T9026, clone DM1A; 1:10,000; RRID:AB_477593). Secondary antibodies were incubated in 5% BLOT-QuickBlocker (G-Biosciences 786-011) as follows: goat anti-mouse HRP conjugate (Jackson Laboratories, 115-035-003; 1:10,000;

RRID:AB_10015289), goat anti-rabbit HRP conjugate (Jackson Laboratories, 111-035-144, 1:10,000; RRID:AB_2307391), goat anti-mouse HRP conjugate (BioRad, 1706516; 1:10,000; RRID:AB_11125547), donkey anti-rabbit HRP conjugate (Amersham, NA9340; 1:10,000; RRID:AB_772191). Detection was performed using WesternBright Quantum detection kit (K-12042-D20). Quantification was performed using FIJI and Microsoft Excel. Image preparation was performed using Adobe Photoshop.

FACS Analysis

For flow cytometry analyses of cell cycle, DNA synthesis and origin licensing wild type and *MCM10+/-* HCT116 and hTERT RPE-1 cells lines were treated as described previously (Matson et al., 2017). Briefly, cells were incubated with 10 uM EdU (Santa Cruz, sc-284628) for 30 minutes before harvesting with trypsin. Cells were chromatin extracted in CSK (10 mM PIPES pH 7.0, 300 mM sucrose, 100 mM NaCl, 3 mM $MgCl_2$ hexahydrate) with 0.5% triton X-100, then fixed in PBS with 4% PFA (Electron Microscopy Services) for 15 minutes. Cells were labeled with 1 μM AF647-azide (Life Technologies, A10277) in 100 mM ascorbic Acid, 1 mM $CuSO_4$, and PBS to detect EdU for 30 minutes, at room temperature. Cells were washed, then incubated with MCM2 antibody 1:200 (BD Biosciences, #610700; RRID:AB_2141952) in 1% BSA in PBS with 0.5% NP-40 for 1 hour at 37°C. Next, cells were washed and labeled with donkey anti-mouse AF488 secondary antibody 1:1,000 (Jackson Immunoresearch, 715-545-150; RRID:AB_2340845) for 1 hour at 37°C. Lastly, cells were washed and incubated in DAPI (Life Technologies D1306) and 100 ng/mL RNAse A (Sigma R6513) overnight at 4°C. Samples were run on an Attune NxT (Beckman Coulter) or LSR II (BD

43

Biosciences) flow cytometer and analyzed with FCS Express 6 (De Novo Software) or FlowJo v10.6.1 and Microsoft Excel.

For flow cytometry analysis of apoptosis, cells were seeded in 6-well plates (HCT116 wild-type at 150,000 cells/well, HCT116 mutants at 200,000-400,000 cells/well, RPE-1 wild-type at 50,000 cells/well, and RPE-1 mutants at 75,000 cells/well) and allowed to proliferate for approximately 72 hours. Cells were collected, washed with 1x PBS twice, and stained using the APC Annexin V apoptosis detection kit (Biolegend 640932) according to the manufacturer's instructions. Samples were analyzed on a FACSCanto A V0730042 (BD Biosciences). Apoptotic cells were identified by annexin V staining while cell viability was determined by PI staining. Data was analyzed using FlowJo v10.6.1 and Microsoft Excel.

DNA Combing

For genome-wide analyses of DNA replication HCT116 cells were plated at 1×10^6 cells per 10 cm plate 48 hours prior to labeling. Cells were incubated with 25 µM IdU (Sigma C6891) for 20 or 30 minutes, rinsed with pre-warmed medium and then incubated with 200 µM CldU (Sigma I7125) for 30 minutes. Approximately 250,000 cells were embedded in 0.5% agarose plugs (NuSieve GTG Agarose, Lonza, 50080) and digested for 48-72 hours in plug digestion solution (10 mM Tris-HCl, pH 7.5, 1% Sarkosyl, 50 mM EDTA and 2 mg/ml Proteinase K). Plugs were subsequently melted in 50 mM MES pH 5.7 (Calbiochem #475893) and digested overnight with β-agarase (NEB M0392). DNA combing was performed using commercially available coverslips (Genomic Vision COV-

44

001). Integrity of combed DNA for all samples was checked via staining with YOYO-1 (Invitrogen Y3601). Combed coverslips were baked at 60°C for 2-4 hours, cooled to room temperature (RT) and stored at -20°C. DNA was denatured in 0.5 M NaOH and 1 M NaCl for 8min at RT. All antibody staining was performed in 2% BSA in PBS-Triton (0.1%). Primary antibodies include rabbit anti-ssDNA (IBL 18731; RRID:AB_494649), mouse anti-BrdU/IdU (BD Biosciences 347580; clone B44; RRID:AB_10015219) and rat anti-BrdU/CldU (Abcam, ab6326; BU1/75 (ICR1); RRID:AB_305426B). Secondary antibodies include goat anti-mouse Cy3.5 (Abcam ab6946; RRID:AB_955045), goat anti-rat Cy5 (Abcam ab6565; RRID:AB_955063) and goat anti-rabbit BV480 (BD Horizon #564879; RRID:AB_2738997). Imaging was performed using Genomic Vision EasyScan service. Image analyses were blinded and used the Genomic Vision FiberStudio software and data/statistical analyses were performed in Microsoft Excel and GraphPad Prism 8.

For telomere specific analyses DNA replication in HCT116 Super-Telomerase, cells were plated as described above. Cells were incubated with 200 μM CldU (Sigma I7125) for 1 hr, rinsed with pre-warmed medium and then grown without label for 2 hrs (repeated 3 additional times). Approximately 500,000 cells were embedded per plug and digested as described above. Plugs were next digested with either RsaI (NEB R0167) or HinfI (NEB R0155) restriction enzyme in 1x NEB CutSmart Buffer to degrade non-telomeric DNA. DNA combing was performed using commercially available coverslips (Genomic Vision COV-001). Integrity of combed DNA for all samples was checked via staining with YOYO-1 (Invitrogen Y3601). Samples were then melted,

45

combed, baked and stored as described above. DNA was denatured in 0.5 M NaOH and 1 M NaCl for 12 min at RT. Telomeres were detected using TelG-Alexa488-conjugated PNA probe (PNA Bio F1008) with a 1:25 dilution in hybridization solution (35% formamide, 10 mM Tris-HCl pH 7.5, 0.5% blocking buffer pH 7.5 (100 mM maleic acid, 150 mM NaCl, 10% Roche blocking reagent #11096176001)). Antibody staining was performed in 3% BSA in PBS-Triton (0.1%). CldU labeled DNA was detected using primary rat anti-CldU (Abcam ab6326; BU1/75 (ICR1); RRID:AB_305426B), followed by secondary goat □nti-rat AF555 (Invitrogen A21434; RRID:AB_2535855) antibodies. Imaging was performed using an EVOS FL imaging system (ThermoFisher AMF43000). Image analyses were blinded and used FIJI and Adobe Photoshop. Statistical analysis was performed using Microsoft Excel.

Clonogenic Survival Assay

For comparison of clonogenic survival without genotoxic stress the specific number of cells plated per well is noted. To assay for sensitivity to genotoxic stress HCT116 cells were plated in 6-well plates according to the plating efficiency of each line. Wild type cells were plated at 500 cells/well, $MCM10^{+/-}$ cells were plated at 800 or 1000 cells/well. After 24 hrs, the medium was removed and replaced with drug containing medium (hydroxyurea, Acros Organics 151680250; mitomycin C, Sigma M4287) or cells were exposed to UV (UVP CL1000 crosslinker) and fresh medium was added. Cells were incubated for 12 to 14 days, washed in PBS, fixed in 10% acetic acid/10% methanol and stained with crystal violet. Colonies reaching a minimum size of 50 cells were counted manually and normalized to the average colony number in untreated wells.

46

Statistical analysis was performed using Microsoft Excel. Plates were imaged using an Epson Expression 1680 scanner.

MTS Cell Proliferation Assay

HCT116 cells were plated at 500 cells per well in 96-well plates and allowed to recover for 24 hrs. Stock solutions of each drug were prepared in sterile 1x PBS, water or DMSO as appropriate and further diluted in growth medium. Cells were allowed to grow for 24 hrs (etoposide, Sigma E1383) or 96 hrs (hydroxyurea, Acros Organics 151680250; mitomycin C, Sigma M4287; aphidicolin, Sigma A0781; cisplatin, Sigma 479306) in drug containing medium and cell viability was measured with the CellTiter 96 Aqueous One Solution Cell Proliferation Assay (Promega G3580) following the manufacturer's instructions. The viability of drug treated cells was normalized to the average viability of the untreated control cells for each cell line. Plates were imaged using a VICTOR^{3}V 1420 Multilabel Counter (Perkin Elmer). Analysis and statistical tests were performed using Microsoft Excel.

Cellular Senescence Assay

HCT116 cells were plated at 2,000-4,000 cells per well and RPE-1 cells were plated at 1,000-1,5000 cells per well in 96-well plates and allowed to recover for three days. The β-galactosidase activity was measured with the 96-Well Cellular Senescence Assay Kit (Cell Biolabs CBA-231) following the manufacturer's instructions with the following modifications. Cell lysates were centrifuged in v-bottom 96-well plates rather than microcentrifuge tubes and total protein concentration was determined using Protein

Assay Dye (BioRad #500-0006) following standard protocols. Plates were imaged using a VICTOR^{3}V 1420 Multilabel Counter (Perkin Elmer). The β-galactosidase activity was normalized to total protein concentration and shown as arbitrary fluorescence units. Analysis and statistical tests were performed using Microsoft Excel.

Telomere Restriction Fragment (TRF) Analysis

Genomic DNA was extracted from ~1 x 10^7 cells using a modified version of the Gentra Puregene Cell Kit cell extraction protocol (Qiagen 158745). Integrity of genomic DNA and absence of contaminating RNA was confirmed via 1% agarose 1x TAE gel electrophoresis. Subsequently, 30-40 µg of genomic DNA was digested with HinfI (NEB R0155) and RsaI (NEB R0167), as described previously (Harvey et al., 2018). For each sample, 8-12 µg of digested genomic DNA was resolved overnight on a 0.7% agarose 1x TBE gel. Gels were depurinated, denatured, and neutralized, followed by overnight capillary transfer to a Hybond-XL membrane (GE Healthcare RPN303S). Telomere probe was labeled using T4 polynucleotide kinase (NEB M0201) and γ-P32-ATP (Perkin Elmer NEG035C) and purified using quick spin columns (Roche 11-273-949-001). Membranes were pre-hybridized for 1 hr with Church buffer at 55°C, then hybridized with a γ-P32-end-labeled telomere probe ($(C_3TA_2)_4$) in Church buffer at 55°C overnight. Membranes were washed three times with 4x SSC and once with 4x SSC + 0.1% SDS, each for 30 min, exposed to a phosphorimaging screen, detected with a Typhoon FLA 9500 imager (University Imaging Centers at the University of Minnesota) and processed using FIJI and Adobe Photoshop. For TRF analyses using telomerase inhibitor, a 10 mM stock solution of BIBR1532 (Tocris #2981) in DMSO was prepared and diluted in

48

appropriate growth medium to a final concentration of 10 µM as described previously (Damm et al., 2001, Jia et al., 2017).

TSQ1 Repeat Incorporation Assay

To generate samples for the TSQ1 incorporation assay (Chow et al., 2018, Diolaiti et al., 2013) three consecutive transient transfections were performed as follows. HCT116 cells were plated at 5×10^5 cells per well in 6-well plates. Approximately 24 hrs later, each well was transfected with equimolar amounts of TSQ1 expression plasmid (pBSK-pU1-hTR TSQ1-termU1; plasmid #1387, gift from Agnel Sfeir) and hTERT expression plasmid (pFLOX-hTERT-Hyg (Taboski et al., 2012), plasmid #LHP333, gift from Lea Harrington) following standard Lipofectamine 3000 protocols (Invitrogen L3000). Cell growth medium was replaced 24 hrs later. Cells were collected and either replated for subsequent transfections or expanded for final sample collection. Samples were prepared as described above for the TRF assay. For each sample, 5-10 µg of digested genomic DNA was blotted onto Hybond-XL membrane using a Bio-Dot Apparatus (BioRad 1706545). Membranes were treated and imaged as described for TRF assays, with the exception of hybridization with TSQ1 specific γ-P32-end-labeled telomere probe $((C_2GCA_2)_4)$. Next, membranes were denatured, neutralized, prehybridized, and re-hybridized with Alu repeat specific γ-P32-end-labeled telomere probe (5'-$GTGATC_2GC_3GC_2TCG_2C_2TC_3A_3GTG$-3'). Membranes were washed and imaged as described. Quantification and statistical analysis was performed using FIJI and Microsoft Excel.

Telomere G-overhang Assay

Samples for G-overhang analyses were prepared as described above for the TRF assay. For each sample, 5-10 µg of digested genomic DNA was separated briefly in 1% agarose 1x TBE gels, the gels were dried, prehybridized for 1hr with Church buffer at 55°C, and hybridized with either C-strand $(C_3TA_2)_4$ or G-strand $(G_3AT_2)_4$ specific γ-P32-end-labeled telomere probes under non-denaturing conditions in Church buffer at 55°C overnight. Gels were washed and imaged as described above for TRF assays. Next, gels were denatured, neutralized, prehybridized, re-hybridized, washed and imaged as described for non-denaturing conditions. To control for differences in loading, band intensities from the native gel were normalized to the corresponding band from the denatured gel. Quantification was performed using FIJI and Microsoft Excel. HCT116 $CTC1^{f/f}$ cells (gift from Carolyn Price) were grown with and without 10 nM 4-hydroxy tamoxifen (Sigma, H7904) to induce Cre activity for the specified number of days prior to sample collection, as described previously (Feng et al., 2017).

Telomere 2D Gel Analysis

The 2D gel analyses of telomeric DNAs were performed as described previously (Wang et al., 2004, Wang et al., 2009, Zellinger et al., 2007). Briefly, samples were collected and prepared as described above for TRF analyses. For S1 nuclease digested samples, 20 µg of RsaI/HinfI digested DNA was digested with 100 U of S1 nuclease (Thermo Scientific #EN0321) for 45 minutes at room temperature. For each sample, 8-12 µg of digested genomic DNA was resolved overnight on a 0.5% agarose 1x TBE gel. Sample lanes were cut out, re-cast and resolved on a 1.2% agarose 1x TBE gel. Gels were

50

treated, transferred to Hybond-XL membrane, labeled and imaged as described above for TRF analyses.

Telomeric Repeat Amplification Protocol (TRAP) Assay

TRAP assays were performed following the manufacturer's protocol for the TRAPeze Telomerase Detection Kit (EMD-Millipore S7700). Briefly, whole cell extracts were prepared using 1x CHAPS lysis buffer and stored at -80□C. Protein concentration was measured using Protein Assay Dye (BioRad #500-0006) in comparison to a BSA (NEB B9000S) standard curve following standard protocols. TRAP reactions were set up using Platinum Taq DNA Polymerase (Invitrogen 10966), resolved on 10% polyacrylamide 0.5x TBE gels, stained for 1 hr with SYBR GOLD (Invitrogen S11494) and detected with a Typhoon FLA 9500 imager and processed using FIJI and Adobe Photoshop.

Immunofluorescence Analyses of Telomeres

For t-FISH (telomere fluorescence in situ hybridization) asynchronous HCT116 populations were incubated for 1 hr in 0.25 µg/mL KaryoMAX colcemid (Gibco 15212-012). Cells were collected and washed in 75mM prewarmed KCl. Cells were then fixed three times in methanol:acetic acid (3:1) by adding fixative solution dropwise with constant gentle agitation by vortex. Following fixation cells were dropped onto microscope slides and metaphase spreads were allowed to dry overnight. Next, slides were rehydrated in 1x PBS, followed by fixation in 3.7% formaldehyde. Slides were then washed twice in 1x PBS, rinsed in ddH2O, dehydrated in an ethanol series (70%, 85%,

51

95%) pre-chilled to -20□C and air dried. FISH was performed with TelC-Cy3 (PNA Bio F1002) and CENPB-Alexa488 (F3004) warmed to 55°C then diluted 1:300 in hybridization buffer (70% formamide, 10mM Tris pH 7.4, 4mM Na_2HPO_4, 0.5mM citric acid, 0.25% TSA blocking reagent (Perkin Elmer FP1012), and 1.25mM MgCl2) preheated to 80°C. Slides were denatured with probe at 80°C, then allowed to incubate at room temperature in a humid chamber. Next, slides were washed twice in PNA wash A (70% formamide, 0.1% BSA, 10 mM Tris pH 7.2) and three times in PNA wash B (100 mM Tris pH 7.2, 150 mM NaCl, 0.1% Tween-20). The second PNA wash B contained DAPI (Life Technologies D1306) at a 1:1000 concentration. Slides were then dehydrated and dried as described above prior to mounting. Slides were blinded prior to imaging and captured using a Zeiss Spinning Disk confocal microscope. Image analyses were blinded and used FIJI and Adobe Photoshop. Statistical analysis was performed using Microsoft Excel.

For CO-FISH (chromosome orientation-fluorescence in situ hybridization) analyses of telomere sister chromatid exchange, HCT116 ST cells were cultured in the presence of BrdU:BrdC (final concentration of 7.5 mM BrdU (MP Biomedicals 100166) and 2.5 mM BrdC (Sigma B5002)) for 12 hrs prior to harvesting. KaryoMAX colcemid (Gibco 15212-012) was added at a concentration of 0.1 µg/mL during the last two hours. CO-FISH was performed as described previously (Doksani and de Lange, 2016) using a TelC-Alexa488-conjugated PNA probe (PNA Bio F1004) followed by a TelG-Cy3-conjugated PNA probe (PNA Bio F1006). Images were captured using a Zeiss Spinning Disk

confocal microscope. Image analyses were blinded and used FIJI and Adobe Photoshop. Statistical analysis was performed using Microsoft Excel.

Telomere C-circle Assay

Genomic DNA for C-circle assays were prepared as described above for the TRF assay. C-circles amplified via rolling circle amplification with or without *phi*29 DNA polymerase (NEB M0269) as described previously (Henson et al., 2017). C-circle reactions were blotted onto Hybond-XL membrane using a Bio-Dot Apparatus (BioRad 1706545). Membranes were treated and imaged as described for TRF assays.

QUANTIFICATION AND STATISTICAL ANALYSIS

Details of Statistical Analysis

Statistical details of experiments including the statistical tests used, value of n, what n represents, dispersion and precision measures (e.g. average, standard deviation), as well as how significance was defined is indicated in each figure and corresponding figure legend. The software used for statistical analysis of each type of experiment is indicated in the corresponding Method Details section.

Quantification of Band/Dot Intensities

Band intensities for western blots, G-overhang assays and TSQ1 assays were quantified using FIJI and Microsoft Excel. Western blot bands were normalized first to the loading control and then to the wild-type value, which was defined as 1.0. For Fig3E, Ub-PCNA was normalized first to unmodified PCNA. Native G-overhang assay bands

were normalized first to the denatured band for each lane and then to the wild type value, which was defined as 1.0. Indicators for peak band intensity on TRF images were determined using FIJI. TSQ1 assay dots were normalized first to the corresponding Alu probe dot signal and then to the wild type value, which was defined as 1.0.

DATA AND CODE AVAILABILITY

This study did not generate or analyze datasets or code.

Supplemental Information Titles and Legends

Figure S1. Mcm10 deficiency increases cell death and sensitivity to MMC.

A) Representative images comparing clonogenic survival of HCT116 wild type and *MCM10*$^{+/-}$ cell lines plated at 1,000 cells per well. Number of days in culture is indicated.

B) Representative flow cytometry plots sorting cells based on propidium iodide and annexin V staining for the quantification of early apoptotic, late apoptotic and dead cells in HCT116 wild type and *MCM10*$^{+/-}$ cell lines.

C) Comparison of drug sensitivity measured by MTS assay comparing average percentage viability in HCT116 wild type and *MCM10*$^{+/-}$ cell lines. Each drug and concentration tested is indicated. Error bars indicate standard deviation and statistical significance was calculated using students *t-test* with *>.05; **>.01, ***>.001; n=6 replicate wells across two biological replicates for all data points.

Figure S2. Characterization of genomic instability in *MCM10*$^{+/-}$ cell populations.

54

A) Representative phase contrast images of early, middle and late passage *MCM10*^{+/-} cell populations.

B) Example karyotypes from late passage HCT116 wild type (top) and mid-passage (middle) or late passage (bottom) *MCM10*^{+/-} cells. Blue arrows indicate expected HCT116 genomic aberrations. Red arrows indicate non-clonal genomic aberrations.

C) TRF analysis comparing early passage HCT116 wild type cells with clonal Mcm10-deficient populations carrying inactivating mutations in one copy of *MCM10* exon 3. Yellow dots indicate the location of peak intensity.

D) Quantification of β-gal activity expressed as arbitrary fluorescence units normalized to total protein for HCT116 wild type (blue) and clonal *MCM10*^{+/-} cell lines (red). Error bars indicate standard deviation and statistical significance was calculated using students *t-test* with *>.05; **>.01, ***>.001; n=3 replicate wells for all data points.

E) Comparison of G-overhang signal in HCT116 wild type, *MCM10*^{+/-} and *CTC1*[f/f] (with and without 4-OHT treatment). As a positive control for increasing G-overhang length, *CTC1*[f/f] cells were treated with or without 10nM 4-OHT for the indicated number of days. Native and denatured gel images probed for the G-strand (using TELC probe) or C-strand (using TELG probe) are shown.

F) Quantification of G-overhang signal in *MCM10*^{+/-} cell lines (red) normalized to HCT116 wild type (blue). Error bars indicate standard deviation; n=3 lanes from independent assays.

G) Quantification of signal free-ends (left) and fragile telomeres (right) in late passage HCT116 wild type (blue) and *MCM10*^{+/-} cells (red). Error bars indicate standard

55

deviation and statistical significance was calculated using students *t-test* with ***<.001; n>86 metaphases per cell line.

H) Flow chart for experiment to generate and analyze PURO-marked *MCM10$^{+/-}$* cell lines.

I) Analysis of a PURO-marked HCT116 *MCM10$^{+/-}$* het #14 cell population tracking average telomere length by TRF (top) and reversion of the exon 14 locus by PCR (bottom). PDs at each time point is indicated. Yellow dots indicate the location of peak intensity.

Figure S3. *CDC45* and *MCM4* deficiency causes haploinsufficiency but not telomere erosion in HCT116 cell lines.

A) Western blot analyses for Mcm10, Cdc45 and Mcm4, with GAPDH loading controls. Quantification of Mcm10, Cdc45 or Mcm4 levels normalized to loading control, relative to the first lane wild-type sample is indicated.

B) Western blot analyses for Cdc45 or Mcm4 with GAPDH as a loading control. Quantification of Cdc45 or Mcm4 levels normalized to loading control, relative to the first lane wild-type sample is indicated.

C) Quantification of growth rate in *CDC45$^{+/-}$* (red) and *MCM4$^{+/-}$* (orange) cell lines normalized to HCT116 wild type cells. For each cell line n=6 replicate wells across three biological replicates; error bars indicate standard deviation and statistical significance was calculated using students *t-test* with *>.05; **>.01, ***>.001.

C) TRF analysis in HCT116 wild type and *CDC45$^{+/-}$* cell lines. Estimated PDs is indicated. Yellow dots indicate the location of peak intensity.

D) TRF analysis in HCT116 wild type and *MCM4*$^{+/-}$ cell lines. Estimated PDs is indicated. Yellow dots indicate the location of peak intensity.

Figure S4. Mcm10 deficiency increases cell death but not activation of senescence pathways in RPE-1 cell lines.

A) Representative flow cytometry plots sorting cells based on propidium iodide and annexin V staining for the quantification of early apoptotic, late apoptotic and dead cells in RPE-1 wild type and *MCM10*$^{+/-}$ cell lines.

B) Average percentage of each population represented by early apoptotic, late apoptotic or dead cells. RPE-1 wild type (blue) and clonal *MCM10*$^{+/-}$ cell lines (red) are shown. Error bars indicate standard deviation and statistical significance was calculated using students *t-test* with *>.05; **>.01, ***>.001; n=4 for all data points.

C) Quantification of β-gal activity expressed as arbitrary fluorescence units normalized to total protein for RPE-1 wild type (blue) and clonal *MCM10*$^{+/-}$ cell lines (red). Error bars indicate standard deviation and statistical significance was calculated using students *t-test* with *>.05; **>.01, ***>.001; n=3 replicate wells for all data points.

Figure S5. Transient or stable overexpression of telomerase lengthens telomeres but does not rescue growth and viability defects.

A) Representative dot-blot images comparing incorporation of mutant TSQ1 telomeric repeats (top) in HCT116 wild type (left) and *MCM10*$^{+/-}$ cell lines (right) with Alu repeats (bottom) as a loading control. Quantification of TSQ1 signal normalized to Alu signal in HCT116 wild type (blue) and *MCM10*$^{+/-}$ cell lines (red). Error bars indicate standard

deviation; n= the number of biological replicates for each cell line where n=6 for WT and *MCM10*$^{+/-}$ clone #8, n=3 for *MCM10*$^{+/-}$ #14.

B) TRF analysis in HCT116 wild type, *MCM10*$^{+/-}$ cell lines and ST derivatives of each parental cell line.

C) Representative TRAP assay comparing telomerase activity in whole cell extracts from HCT116 wild type (left) and *MCM10*$^{+/-}$ ST cell lines (right). The internal PCR control at 36bp and telomerase products beginning at 50bp are noted. For each cell line, two concentrations of cell extract were used representing a 10-fold dilution.

D) Western blot analyses of whole cell extracts from HCT116 ST wild type and *MCM10*$^{+/-}$ cell lines for Mcm10 with Tubulin as a loading control. Quantification of Mcm10 levels normalized to loading control, relative to the first lane wild-type ST3 sample is indicated.

E) Average proliferation rate in HCT116 wild type, *MCM10*$^{+/-}$ and ST cell lines normalized to HCT116 wild type cells. For each cell line n=4 replicate wells across two biological replicates; error bars indicate standard deviation and statistical significance was calculated using students *t-test* with *>.05; **>.01, ***>.001.

F) Comparison of clonogenic survival in HCT116 wild type, *MCM10*$^{+/-}$ and ST cell lines. The number of cells plated per well is indicated.

Figure S6. Spontaneous reversion of *MCM10+/-* ST cells rescues t-complex accumulation and proliferation rate.

A) Dot-blot comparing C-circle levels in HCT116 wild type, *MCM10*$^{+/-}$ and Super-Telomerase derivative cell lines, with U2OS cells used as a positive control. Reactions without phi-29 DNA polymerase demonstrate the background C-circle levels.

B) (Top left) Diagram of double-stranded telomere restriction fragment (ds-TRF), telomere circle (t-circle) and telomere complex (t-complex) DNA species from 2D TRF gel electrophoresis. (Right) Representative comparison of 2D TRF gel electrophoresis in HCT116 wild type, $MCM10^{+/-}$ and reverted ST cell lines. (Bottom left) Genotyping PCR for exon 14 in cell populations showing alleles that have one *loxP* site 3' of exon 14 (upper band) or a *loxP* scar (lower band), as well as exon 14 reverted alleles that have retained or lost the 3' *loxP* site. A faint non-specific band can also be detected (asterisk).

C) Average proliferation rate in HCT116 wild type, $MCM10^{+/-}$ and reverted ST cell lines normalized to HCT116 wild type ST3. For each cell line n=5 replicate wells across two biological replicates; error bars indicate standard deviation and statistical significance was calculated using students *t-test* with *>.05; **>.01, ***>.001.

References

ARNOULT, N., SCHLUTH-BOLARD, C., LETESSIER, A., DRASCOVIC, I., BOUARICH-BOURIMI, R., CAMPISI, J., KIM, S. H., BOUSSOUAR, A., OTTAVIANI, A., MAGDINIER, F., GILSON, E. & LONDONO-VALLEJO, A. 2010. Replication timing of human telomeres is chromosome arm-specific, influenced by subtelomeric structures and connected to nuclear localization. *PLoS Genet,* 6, e1000920.

BARTHA, I., DI IULIO, J., VENTER, J. C. & TELENTI, A. 2018. Human gene essentiality. *Nat Rev Genet,* 19, 51-62.

BAXLEY, R. M. & BIELINSKY, A. K. 2017. Mcm10: A Dynamic Scaffold at Eukaryotic Replication Forks. *Genes (Basel),* 8.

BECKER, J. R., GALLO, D., LEUNG, W., CROISSANT, T., THU, Y. M., NGUYEN, H. D., STARR, T. K., BROWN, G. W. & BIELINSKY, A. K. 2018. Flap endonuclease overexpression drives genome instability and DNA damage hypersensitivity in a PCNA-dependent manner. *Nucleic Acids Res,* 46, 5634-5650.

BIANCO, J. N., BERGOGLIO, V., LIN, Y. L., PILLAIRE, M. J., SCHMITZ, A. L., GILHODES, J., LUSQUE, A., MAZIERES, J., LACROIX-TRIKI, M., ROUMELIOTIS, T. I., CHOUDHARY, J., MOREAUX, J., HOFFMANN, J. S., TOURRIERE, H. & PASERO, P. 2019. Overexpression of Claspin and Timeless protects cancer cells from replication stress in a checkpoint-independent manner. *Nat Commun,* 10, 910.

BIELINSKY, A. K. 2003. Replication origins: why do we need so many? *Cell Cycle,* 2, 307-9.

BLOW, J. J., GE, X. Q. & JACKSON, D. A. 2011. How dormant origins promote complete genome replication. *Trends Biochem Sci,* 36, 405-14.

BOOS, D. & FERREIRA, P. 2019. Origin Firing Regulations to Control Genome Replication Timing. *Genes (Basel),* 10.

BRINKMAN, E. K., CHEN, T., AMENDOLA, M. & VAN STEENSEL, B. 2014. Easy quantitative assessment of genome editing by sequence trace decomposition. *Nucleic Acids Res,* 42, e168.

CASEY, J. P., NOBBS, M., MCGETTIGAN, P., LYNCH, S. & ENNIS, S. 2012. Recessive mutations in MCM4/PRKDC cause a novel syndrome involving a primary immunodeficiency and a disorder of DNA repair. *J Med Genet,* 49, 242-5.

CHADHA, G. S., GAMBUS, A., GILLESPIE, P. J. & BLOW, J. J. 2016. Xenopus Mcm10 is a CDK-substrate required for replication fork stability. *Cell Cycle,* 15, 2183-2195.

CHOW, T. T., SHI, X., WEI, J. H., GUAN, J., STADLER, G., HUANG, B. & BLACKBURN, E. H. 2018. Local enrichment of HP1alpha at telomeres alters their structure and regulation of telomere protection. *Nat Commun,* 9, 3583.

COTTINEAU, J., KOTTEMANN, M. C., LACH, F. P., KANG, Y. H., VELY, F., DEENICK, E. K., LAZAROV, T., GINEAU, L., WANG, Y., FARINA, A., CHANSEL, M., LORENZO, L., PIPEROGLOU, C., MA, C. S., NITSCHKE, P., BELKADI, A., ITAN, Y., BOISSON, B., JABOT-HANIN, F., PICARD, C., BUSTAMANTE, J., EIDENSCHENK, C., BOUCHERIT, S., ALADJIDI, N., LACOMBE, D., BARAT, P., QASIM, W., HURST, J. A., POLLARD, A. J., UHLIG, H. H., FIESCHI, C.,

MICHON, J., BERMUDEZ, V. P., ABEL, L., DE VILLARTAY, J. P., GEISSMANN, F., TANGYE, S. G., HURWITZ, J., VIVIER, E., CASANOVA, J. L., SMOGORZEWSKA, A. & JOUANGUY, E. 2017. Inherited GINS1 deficiency underlies growth retardation along with neutropenia and NK cell deficiency. *J Clin Invest,* 127**,** 1991-2006.

CRISTOFARI, G. & LINGNER, J. 2006. Telomere length homeostasis requires that telomerase levels are limiting. *EMBO J,* 25**,** 565-74.

CUI, F., HU, J., NING, S., TAN, J. & TANG, H. 2018. Overexpression of MCM10 promotes cell proliferation and predicts poor prognosis in prostate cancer. *Prostate.*

DAMM, K., HEMMANN, U., GARIN-CHESA, P., HAUEL, N., KAUFFMANN, I., PRIEPKE, H., NIESTROJ, C., DAIBER, C., ENENKEL, B., GUILLIARD, B., LAURITSCH, I., MULLER, E., PASCOLO, E., SAUTER, G., PANTIC, M., MARTENS, U. M., WENZ, C., LINGNER, J., KRAUT, N., RETTIG, W. J. & SCHNAPP, A. 2001. A highly selective telomerase inhibitor limiting human cancer cell proliferation. *EMBO J,* 20**,** 6958-68.

DAS, M., PRASAD, S. B., YADAV, S. S., GOVARDHAN, H. B., PANDEY, L. K., SINGH, S., PRADHAN, S. & NARAYAN, G. 2013. Over expression of minichromosome maintenance genes is clinically correlated to cervical carcinogenesis. *PLoS One,* 8**,** e69607.

DEBATISSE, M., LE TALLEC, B., LETESSIER, A., DUTRILLAUX, B. & BRISON, O. 2012. Common fragile sites: mechanisms of instability revisited. *Trends Genet,* 28**,** 22-32.

DILLEY, R. L., VERMA, P., CHO, N. W., WINTERS, H. D., WONDISFORD, A. R. & GREENBERG, R. A. 2016. Break-induced telomere synthesis underlies alternative telomere maintenance. *Nature,* 539**,** 54-58.

DING, H., SCHERTZER, M., WU, X., GERTSENSTEIN, M., SELIG, S., KAMMORI, M., POURVALI, R., POON, S., VULTO, I., CHAVEZ, E., TAM, P. P., NAGY, A. & LANSDORP, P. M. 2004. Regulation of murine telomere length by Rtel: an essential gene encoding a helicase-like protein. *Cell,* 117**,** 873-86.

DIOLAITI, M. E., CIMINI, B. A., KAGEYAMA, R., CHARLES, F. A. & STOHR, B. A. 2013. In situ visualization of telomere elongation patterns in human cells. *Nucleic Acids Res,* 41**,** e176.

DOKSANI, Y. & DE LANGE, T. 2016. Telomere-Internal Double-Strand Breaks Are Repaired by Homologous Recombination and PARP1/Lig3-Dependent End-Joining. *Cell Rep,* 17**,** 1646-1656.

DOUGLAS, M. E., ALI, F. A., COSTA, A. & DIFFLEY, J. F. X. 2018. The mechanism of eukaryotic CMG helicase activation. *Nature,* 555**,** 265-268.

DURKIN, S. G. & GLOVER, T. W. 2007. Chromosome fragile sites. *Annu Rev Genet,* 41**,** 169-92.

EVRIN, C., CLARKE, P., ZECH, J., LURZ, R., SUN, J., UHLE, S., LI, H., STILLMAN, B. & SPECK, C. 2009. A double-hexameric MCM2-7 complex is loaded onto origin DNA during licensing of eukaryotic DNA replication. *Proc Natl Acad Sci U S A,* 106**,** 20240-5.

FALI, T., PAPAGNO, L., BAYARD, C., MOULOUD, Y., BODDAERT, J., SAUCE, D. & APPAY, V. 2019. New Insights into Lymphocyte Differentiation and Aging from

Telomere Length and Telomerase Activity Measurements. *J Immunol,* 202**,** 1962-1969.

FALQUET, B. & RASS, U. 2019. Structure-Specific Endonucleases and the Resolution of Chromosome Underreplication. *Genes (Basel),* 10.

FATOBA, S. T., TOGNETTI, S., BERTO, M., LEO, E., MULVEY, C. M., GODOVAC-ZIMMERMANN, J., POMMIER, Y. & OKOROKOV, A. L. 2013. Human SIRT1 regulates DNA binding and stability of the Mcm10 DNA replication factor via deacetylation. *Nucleic Acids Res,* 41**,** 4065-79.

FENG, X., HSU, S. J., KASBEK, C., CHAIKEN, M. & PRICE, C. M. 2017. CTC1-mediated C-strand fill-in is an essential step in telomere length maintenance. *Nucleic Acids Res,* 45**,** 4281-4293.

GARCIA-ARAGONCILLO, E., CARRILLO, J., LALLI, E., AGRA, N., GOMEZ-LOPEZ, G., PESTANA, A. & ALONSO, J. 2008. DAX1, a direct target of EWS/FLI1 oncoprotein, is a principal regulator of cell-cycle progression in Ewing's tumor cells. *Oncogene,* 27**,** 6034-43.

GINEAU, L., COGNET, C., KARA, N., LACH, F. P., DUNNE, J., VETURI, U., PICARD, C., TROUILLET, C., EIDENSCHENK, C., AOUFOUCHI, S., ALCAIS, A., SMITH, O., GEISSMANN, F., FEIGHERY, C., ABEL, L., SMOGORZEWSKA, A., STILLMAN, B., VIVIER, E., CASANOVA, J. L. & JOUANGUY, E. 2012. Partial MCM4 deficiency in patients with growth retardation, adrenal insufficiency, and natural killer cell deficiency. *J Clin Invest,* 122**,** 821-32.

HANNA, S., BEZIAT, V., JOUANGUY, E., CASANOVA, J. L. & ETZIONI, A. 2015. A homozygous mutation of RTEL1 in a child presenting with an apparently isolated natural killer cell deficiency. *J Allergy Clin Immunol,* 136**,** 1113-4.

HARVEY, A., MIELKE, N., GRIMSTEAD, J. W., JONES, R. E., NGUYEN, T., MUELLER, M., BAIRD, D. M. & HENDRICKSON, E. A. 2018. PARP1 is required for preserving telomeric integrity but is dispensable for A-NHEJ. *Oncotarget,* 9**,** 34821-34837.

HENSON, J. D., CAO, Y., HUSCHTSCHA, L. I., CHANG, A. C., AU, A. Y., PICKETT, H. A. & REDDEL, R. R. 2009. DNA C-circles are specific and quantifiable markers of alternative-lengthening-of-telomeres activity. *Nat Biotechnol,* 27**,** 1181-5.

HENSON, J. D., LAU, L. M., KOCH, S., MARTIN LA ROTTA, N., DAGG, R. A. & REDDEL, R. R. 2017. The C-Circle Assay for alternative-lengthening-of-telomeres activity. *Methods,* 114**,** 74-84.

HUANG, N., LEE, I., MARCOTTE, E. M. & HURLES, M. E. 2010. Characterising and predicting haploinsufficiency in the human genome. *PLoS Genet,* 6**,** e1001154.

HUGHES, C. R., GUASTI, L., MEIMARIDOU, E., CHUANG, C. H., SCHIMENTI, J. C., KING, P. J., COSTIGAN, C., CLARK, A. J. & METHERELL, L. A. 2012. MCM4 mutation causes adrenal failure, short stature, and natural killer cell deficiency in humans. *J Clin Invest,* 122**,** 814-20.

JAFRI, M. A., ANSARI, S. A., ALQAHTANI, M. H. & SHAY, J. W. 2016. Roles of telomeres and telomerase in cancer, and advances in telomerase-targeted therapies. *Genome Med,* 8**,** 69.

JIA, P., CHASTAIN, M., ZOU, Y., HER, C. & CHAI, W. 2017. Human MLH1 suppresses the insertion of telomeric sequences at intra-chromosomal sites in telomerase-expressing cells. *Nucleic Acids Res,* 45**,** 1219-1232.
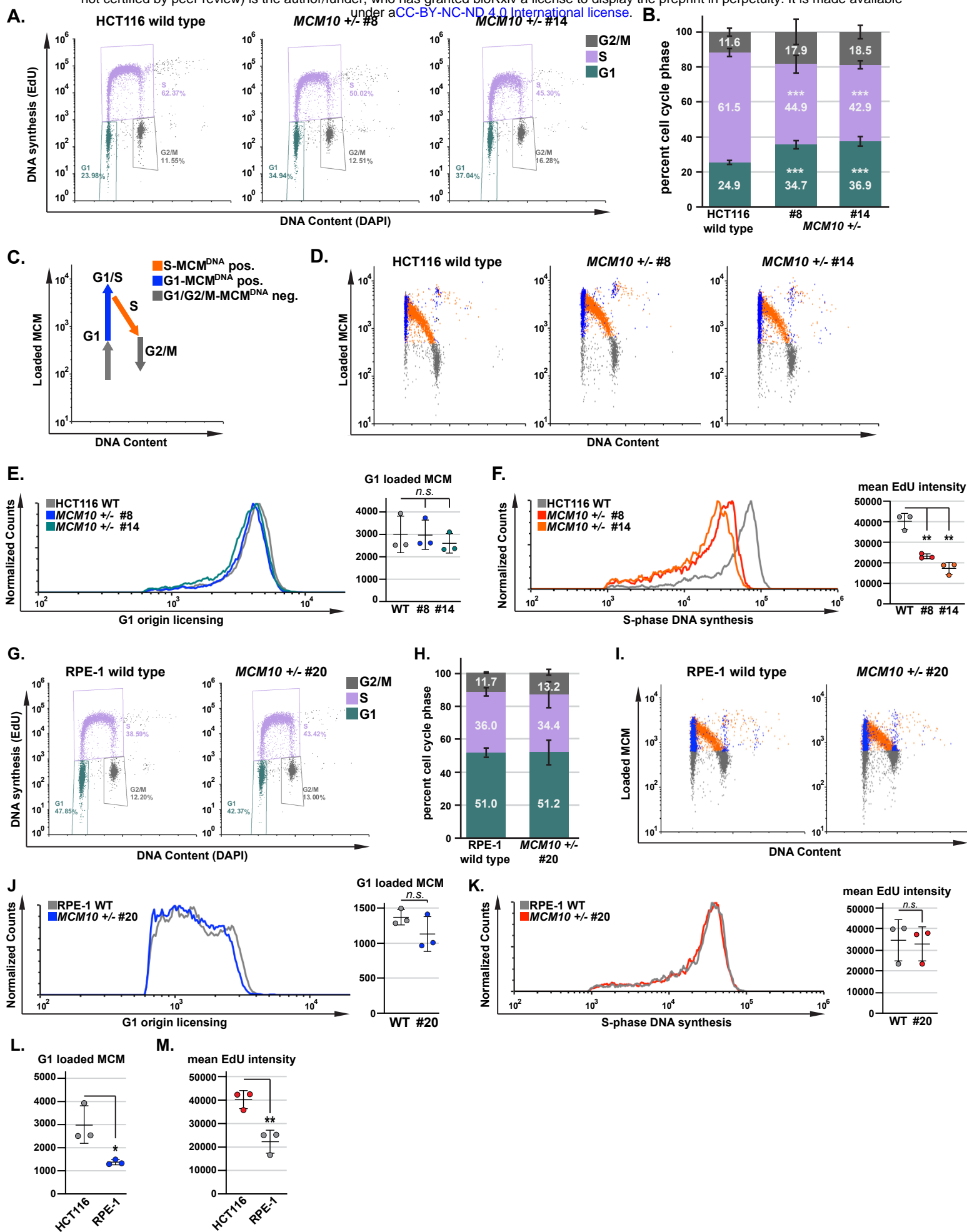
KOHLI, M., RAGO, C., LENGAUER, C., KINZLER, K. W. & VOGELSTEIN, B. 2004. Facile methods for generating human somatic cell gene knockouts using recombinant adeno-associated viruses. *Nucleic Acids Res,* 32**,** e3.

LANGSTON, L. D., MAYLE, R., SCHAUER, G. D., YURIEVA, O., ZHANG, D., YAO, N. Y., GEORGESCU, R. E. & O'DONNELL, M. E. 2017. Mcm10 promotes rapid isomerization of CMG-DNA for replisome bypass of lagging strand DNA blocks. *Elife,* 6.

LANGSTON, L. D. & O'DONNELL, M. E. 2019. An explanation for origin unwinding in eukaryotes. *Elife,* 8.

LEE, S. & SCHMITT, C. A. 2019. The dynamic nature of senescence in cancer. *Nat Cell Biol,* 21**,** 94-101.

LEUNG, W., BAXLEY, R. M., MOLDOVAN, G. L. & BIELINSKY, A. K. 2018. Mechanisms of DNA Damage Tolerance: Post-Translational Regulation of PCNA. *Genes (Basel),* 10.

LIM, H. J., JEON, Y., JEON, C. H., KIM, J. H. & LEE, H. 2011. Targeted disruption of Mcm10 causes defective embryonic cell proliferation and early embryo lethality. *Biochim Biophys Acta,* 1813**,** 1777-83.

LOOKE, M., MALONEY, M. F. & BELL, S. P. 2017. Mcm10 regulates DNA replication elongation by stimulating the CMG replicative helicase. *Genes Dev,* 31**,** 291-305.

LUKUSA, T. & FRYNS, J. P. 2008. Human chromosome fragility. *Biochim Biophys Acta,* 1779**,** 3-16.

MAESTRONI, L., MATMATI, S. & COULON, S. 2017. Solving the Telomere Replication Problem. *Genes (Basel),* 8.

MARGALEF, P., KOTSANTIS, P., BOREL, V., BELLELLI, R., PANIER, S. & BOULTON, S. J. 2018. Stabilization of Reversed Replication Forks by Telomerase Drives Telomere Catastrophe. *Cell,* 172**,** 439-453 e14.

MARTINEZ, P. & BLASCO, M. A. 2015. Replicating through telomeres: a means to an end. *Trends Biochem Sci,* 40**,** 504-15.

MASON-OSANN, E., GALI, H. & FLYNN, R. L. 2019. Resolving Roadblocks to Telomere Replication. *Methods Mol Biol,* 1999**,** 31-57.

MATSON, J. P., DUMITRU, R., CORYELL, P., BAXLEY, R. M., CHEN, W., TWAROSKI, K., WEBBER, B. R., TOLAR, J., BIELINSKY, A. K., PURVIS, J. E. & COOK, J. G. 2017. Rapid DNA replication origin licensing protects stem cell pluripotency. *Elife,* 6.

MAYLE, R., LANGSTON, L., MOLLOY, K. R., ZHANG, D., CHAIT, B. T. & O'DONNELL, M. E. 2019. Mcm10 has potent strand-annealing activity and limits translocase-mediated fork regression. *Proc Natl Acad Sci U S A,* 116**,** 798-803.

MIOTTO, B., CHIBI, M., XIE, P., KOUNDRIOUKOFF, S., MOOLMAN-SMOOK, H., PUGH, D., DEBATISSE, M., HE, F., ZHANG, L. & DEFOSSEZ, P. A. 2014. The RBBP6/ZBTB38/MCM10 axis regulates DNA replication and common fragile site stability. *Cell Rep,* 7**,** 575-87.

MOTEGI, A., LIAW, H. J., LEE, K. Y., ROEST, H. P., MAAS, A., WU, X., MOINOVA, H., MARKOWITZ, S. D., DING, H., HOEIJMAKERS, J. H. & MYUNG, K. 2008. Polyubiquitination of proliferating cell nuclear antigen by HLTF and SHPRH prevents genomic instability from stalled replication forks. *Proc Natl Acad Sci U S A,* 105**,** 12411-6.

MOYER, S. E., LEWIS, P. W. & BOTCHAN, M. R. 2006. Isolation of the Cdc45/Mcm2-7/GINS (CMG) complex, a candidate for the eukaryotic DNA replication fork helicase. *Proc Natl Acad Sci U S A,* 103**,** 10236-10241.

MRASEK, K., SCHODER, C., TEICHMANN, A. C., BEHR, K., FRANZE, B., WILHELM, K., BLAUROCK, N., CLAUSSEN, U., LIEHR, T. & WEISE, A. 2010. Global screening and extended nomenclature for 230 aphidicolin-inducible fragile sites, including 61 yet unreported ones. *Int J Oncol,* 36**,** 929-40.

NABETANI, A. & ISHIKAWA, F. 2009. Unusual telomeric DNAs in human telomerase-negative immortalized cells. *Mol Cell Biol,* 29**,** 703-13.

O'SULLIVAN, R. J., ARNOULT, N., LACKNER, D. H., OGANESIAN, L., HAGGBLOM, C., CORPET, A., ALMOUZNI, G. & KARLSEDER, J. 2014. Rapid induction of alternative lengthening of telomeres by depletion of the histone chaperone ASF1. *Nat Struct Mol Biol,* 21**,** 167-74.

OUYANG, Q., BAERLOCHER, G., VULTO, I. & LANSDORP, P. M. 2007. Telomere length in human natural killer cell subsets. *Ann N Y Acad Sci,* 1106**,** 240-52.

PAN, X., DROSOPOULOS, W. C., SETHI, L., MADIREDDY, A., SCHILDKRAUT, C. L. & ZHANG, D. 2017. FANCM, BRCA1, and BLM cooperatively resolve the replication stress at the ALT telomeres. *Proc Natl Acad Sci U S A,* 114**,** E5940-E5949.

PAULSON, C. N., JOHN, K., BAXLEY, R. M., KURNIAWAN, F., ORELLANA, K., FRANCIS, R., SOBECK, A., EICHMAN, B. F., CHAZIN, W. J., AIHARA, H., GEORG, G. I., HAWKINSON, J. E. & BIELINSKY, A. K. 2019. The anti-parasitic agent suramin and several of its analogues are inhibitors of the DNA binding protein Mcm10. *Open Biol,* 9**,** 190117.

PIQUERET-STEPHAN, L., RICOUL, M., HEMPEL, W. M. & SABATIER, L. 2016. Replication Timing of Human Telomeres is Conserved during Immortalization and Influenced by Respective Subtelomeres. *Sci Rep,* 6**,** 32510.

RAN, F. A., HSU, P. D., WRIGHT, J., AGARWALA, V., SCOTT, D. A. & ZHANG, F. 2013. Genome engineering using the CRISPR-Cas9 system. *Nat Protoc,* 8**,** 2281-2308.

REMUS, D., BEURON, F., TOLUN, G., GRIFFITH, J. D., MORRIS, E. P. & DIFFLEY, J. F. 2009. Concerted loading of Mcm2-7 double hexamers around DNA during DNA replication origin licensing. *Cell,* 139**,** 719-30.

RIVERA, T., HAGGBLOM, C., COSCONATI, S. & KARLSEDER, J. 2017. A balance between elongation and trimming regulates telomere stability in stem cells. *Nat Struct Mol Biol,* 24**,** 30-39.

RODRIGUEZ-ACEBES, S., MOURON, S. & MENDEZ, J. 2018. Uncoupling fork speed and origin activity to identify the primary cause of replicative stress phenotypes. *J Biol Chem,* 293**,** 12855-12861.

ROMAGNANI, C., JUELKE, K., FALCO, M., MORANDI, B., D'AGOSTINO, A., COSTA, R., RATTO, G., FORTE, G., CARREGA, P., LUI, G., CONTE, R., STROWIG, T., MORETTA, A., MUNZ, C., THIEL, A., MORETTA, L. & FERLAZZO, G. 2007. CD56brightCD16- killer Ig-like receptor- NK cells display longer telomeres and acquire features of CD56dim NK cells upon activation. *J Immunol,* 178**,** 4947-55.

SCHMUTZ, I., TIMASHEV, L., XIE, W., PATEL, D. J. & DE LANGE, T. 2017. TRF2 binds branched DNA to safeguard telomere integrity. *Nat Struct Mol Biol,* 24**,** 734-742.

SENFTER, D., ERKAN, E. P., OZER, E., JUNGWIRTH, G., MADLENER, S., KOOL, M., STROBEL, T., SAYDAM, N. & SAYDAM, O. 2017. Overexpression of minichromosome maintenance protein 10 in medulloblastoma and its clinical implications. *Pediatr Blood Cancer,* 64.

SFEIR, A., KOSIYATRAKUL, S. T., HOCKEMEYER, D., MACRAE, S. L., KARLSEDER, J., SCHILDKRAUT, C. L. & DE LANGE, T. 2009. Mammalian telomeres resemble fragile sites and require TRF1 for efficient replication. *Cell,* 138**,** 90-103.

SHARMA, A., KAUR, M., KAR, A., RANADE, S. M. & SAXENA, S. 2010. Ultraviolet radiation stress triggers the down-regulation of essential replication factor Mcm10. *J Biol Chem,* 285**,** 8352-62.

SHAY, J. W. 2016. Role of Telomeres and Telomerase in Aging and Cancer. *Cancer Discov,* 6**,** 584-93.

SOBINOFF, A. P., ALLEN, J. A., NEUMANN, A. A., YANG, S. F., WALSH, M. E., HENSON, J. D., REDDEL, R. R. & PICKETT, H. A. 2017. BLM and SLX4 play opposing roles in recombination-dependent replication at human telomeres. *EMBO J,* 36**,** 2907-2919.

STEWART, J. A., WANG, Y., ACKERSON, S. M. & SCHUCK, P. L. 2018. Emerging roles of CST in maintaining genome stability and human disease. *Front Biosci (Landmark Ed),* 23**,** 1564-1586.

TABOSKI, M. A., SEALEY, D. C., DORRENS, J., TAYADE, C., BETTS, D. H. & HARRINGTON, L. 2012. Long telomeres bypass the requirement for telomere maintenance in human tumorigenesis. *Cell Rep,* 1**,** 91-8.

THOMPSON, E. L., YEO, J. E., LEE, E. A., KAN, Y., RAGHUNANDAN, M., WIEK, C., HANENBERG, H., SCHARER, O. D., HENDRICKSON, E. A. & SOBECK, A. 2017. FANCI and FANCD2 have common as well as independent functions during the cellular replication stress response. *Nucleic Acids Res,* 45**,** 11837-11857.

THU, Y. M. & BIELINSKY, A. K. 2013. Enigmatic roles of Mcm10 in DNA replication. *Trends Biochem Sci,* 38**,** 184-94.

TOMLINSON, R. L., ZIEGLER, T. D., SUPAKORNDEJ, T., TERNS, R. M. & TERNS, M. P. 2006. Cell cycle-regulated trafficking of human telomerase to telomeres. *Mol Biol Cell,* 17**,** 955-65.

URINGA, E. J., LISAINGO, K., PICKETT, H. A., BRIND'AMOUR, J., ROHDE, J. H., ZELENSKY, A., ESSERS, J. & LANSDORP, P. M. 2012. RTEL1 contributes to DNA replication and repair and telomere maintenance. *Mol Biol Cell,* 23**,** 2782-92.

VANNIER, J. B., PAVICIC-KALTENBRUNNER, V., PETALCORIN, M. I., DING, H. & BOULTON, S. J. 2012. RTEL1 dismantles T loops and counteracts telomeric G4-DNA to maintain telomere integrity. *Cell,* 149**,** 795-806.

VANNIER, J. B., SANDHU, S., PETALCORIN, M. I., WU, X., NABI, Z., DING, H. & BOULTON, S. J. 2013. RTEL1 is a replisome-associated helicase that promotes telomere and genome-wide replication. *Science,* 342**,** 239-42.

WANG, M., XIE, S., YUAN, W., XIE, T., JAMAL, M., HUANG, J., YIN, Q., SONG, H. & ZHANG, Q. 2019. Minichromosome maintenance protein 10 as a marker for proliferation and prognosis in lung cancer. *Int J Oncol.*

WANG, R. C., SMOGORZEWSKA, A. & DE LANGE, T. 2004. Homologous recombination generates T-loop-sized deletions at human telomeres. *Cell,* 119**,** 355-68.

WANG, Y., GHOSH, G. & HENDRICKSON, E. A. 2009. Ku86 represses lethal telomere deletion events in human somatic cells. *Proc Natl Acad Sci U S A,* 106**,** 12430-5.

WASSERMAN, M. R., SCHAUER, G. D., O'DONNELL, M. E. & LIU, S. 2019. Replication Fork Activation Is Enabled by a Single-Stranded DNA Gate in CMG Helicase. *Cell,* 178**,** 600-611 e16.

WATASE, G., TAKISAWA, H. & KANEMAKI, M. T. 2012. Mcm10 plays a role in functioning of the eukaryotic replicative DNA helicase, Cdc45-Mcm-GINS. *Curr Biol,* 22**,** 343-9.

WONG, J. M. & COLLINS, K. 2006. Telomerase RNA level limits telomere maintenance in X-linked dyskeratosis congenita. *Genes Dev,* 20**,** 2848-58.

WRIGHT, W. E., SHAY, J. W. & PIATYSZEK, M. A. 1995. Modifications of a telomeric repeat amplification protocol (TRAP) result in increased reliability, linearity and sensitivity. *Nucleic Acids Res,* 23**,** 3794-5.

WU, C., ZHU, J. & ZHANG, X. 2012. Integrating gene expression and protein-protein interaction network to prioritize cancer-associated genes. *BMC Bioinformatics,* 13**,** 182.

YEELES, J. T., DEEGAN, T. D., JANSKA, A., EARLY, A. & DIFFLEY, J. F. 2015. Regulated eukaryotic DNA replication origin firing with purified proteins. *Nature,* 519**,** 431-5.

ZELLINGER, B., AKIMCHEVA, S., PUIZINA, J., SCHIRATO, M. & RIHA, K. 2007. Ku suppresses formation of telomeric circles and alternative telomere lengthening in Arabidopsis. *Mol Cell,* 27**,** 163-9.

ZHANG, J. M., YADAV, T., OUYANG, J., LAN, L. & ZOU, L. 2019. Alternative Lengthening of Telomeres through Two Distinct Break-Induced Replication Pathways. *Cell Rep,* 26**,** 955-968 e3.

ZHONG, Y., NELLIMOOTTIL, T., PEACE, J. M., KNOTT, S. R., VILLWOCK, S. K., YEE, J. M., JANCUSKA, J. M., REGE, S., TECKLENBURG, M., SCLAFANI, R. A., TAVARE, S. & APARICIO, O. M. 2013. The level of origin firing inversely affects the rate of replication fork progression. *J Cell Biol,* 201**,** 373-83.

A.

B. genotyping PCR

C. HCT116 / RPE-1

D.

proliferation rate relative to WT — *exon 14* / *exon 3* — HCT116 *MCM10 +/-*

E.

proliferation rate relative to WT — *exon 3* — RPE-1 *MCM10 +/-*

F.

HCT116 wild type / *MCM10 +/-* #8 / *MCM10 +/-* #14 — cells per well: 1,000 / 1,250 / 1,500

G.

% clonogenic survival — HCT116 wild type / #8 / #14 *MCM10 +/-*

A.

B.

C.

A. early, mid, late

B.

HCT116 WT (~200 PD)

MCM10 +/- (~25 PD)
clone#8 -- [transl(5;8),-21,inv(21)]

MCM10 +/- (~100 PD)
clone #8 -- [transl (3), del (5), del (11), transl (12)]

C. MCM10 +/- exon3 — WT, 1, 4, 26

D. β-gal activity units (x10^4) — HCT116 WT, MCM10 +/- #8, MCM10 +/- #14

E. wild type, MCM10 +/- #8 #14, CTC1 f/f - 4-OHT / + 4-OHT, days 2 5 8 / 5 8
native, denatured — G-strand (TELC probe)
native, denatured — C-strand (TELG probe)

F. G-overhang signal (normalized to wild type) — WT, #8, #14, MCM10 +/-

G. Signal Free Ends, Fragile Telomeres — SFE / chromosome ends, fragile telomeres / chromosome ends — WT, #8, #14, MCM10 +/-

H.
Five early or mid passage MCM10 +/- #8 or #14 populations
↓
PURO plasmid transfection
↓
PURO drug selection
↓
Expand PURO-resistant population
↓
*Plate populations to begin time course (PD = 0)
(Begin weekly sample collection)*
↓
Repeat PURO selection of all populations (~PD = 20-30)
↓
Repeat PURO selection of all populations (~PD = 70-80)

I. MCM10 +/- #14 PURO-marked — PD: 5 10 15 20 26 32 37 43 48 54 58 64 70 75 79 86 — genotyping PCR

A.

B.

C.

D.

E.

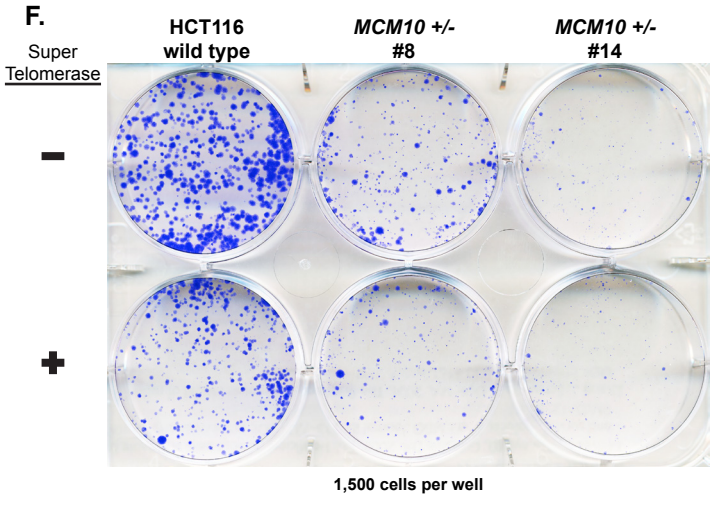
F.

A.
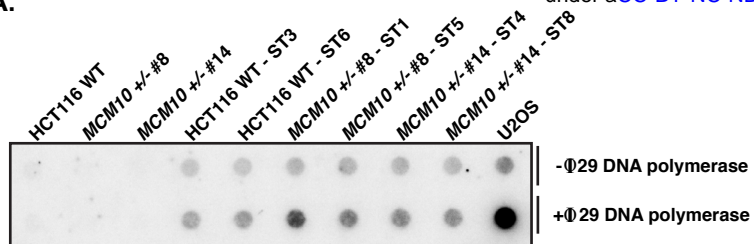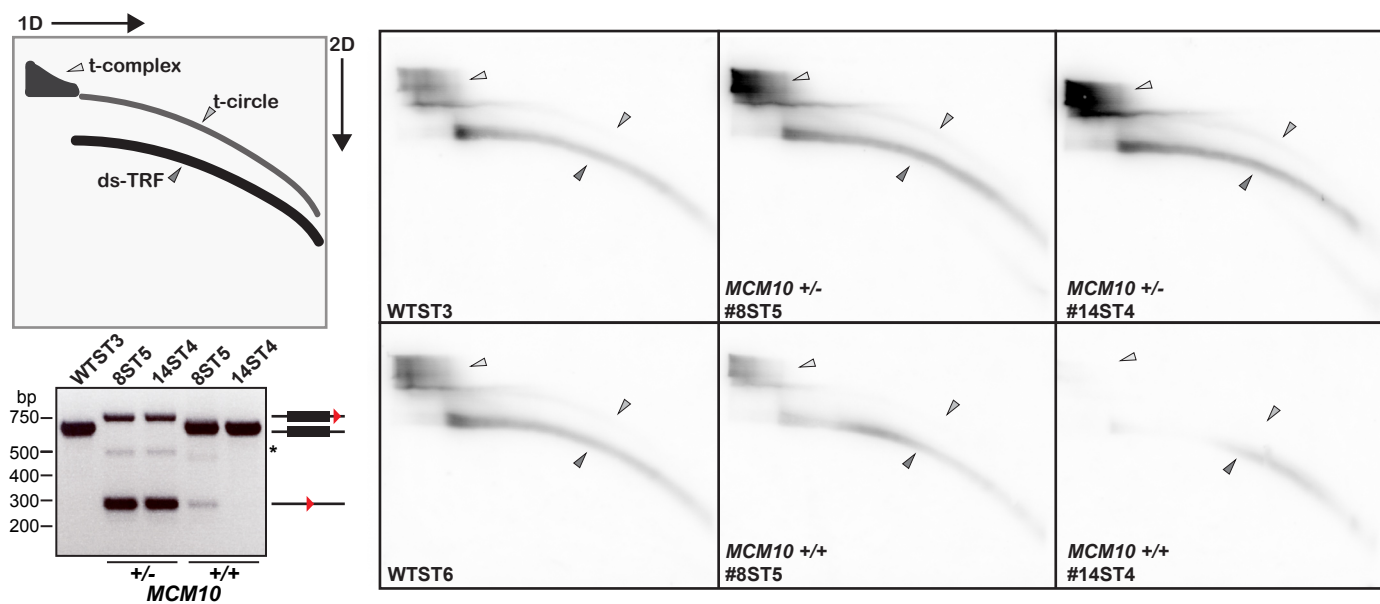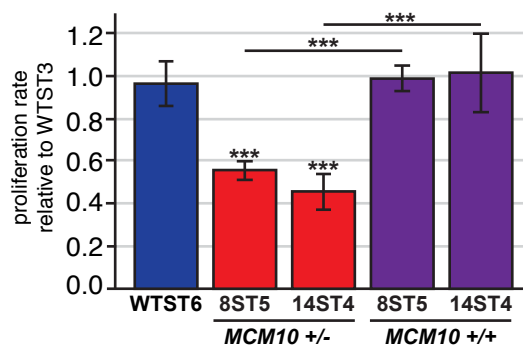

-Φ29 DNA polymerase

+Φ29 DNA polymerase

B.

C.

HCT116 expected	Durking & Glover, 2007 [Durkin, 2007 #60]	Lukusa & Fryns, 2008 [Lukusa, 2008 #62]	Mrasek et al., 2010 [Mrasek, 2010 #61]
dup(10)(q24.1q26.3)	Yes - 10q26.3	No	No
der(16)t(8;16)(q13;p13.3)	No	No	Yes - 8q13 (FRA8F)
der(18)t(17;18)(q21;p11.2)	No	No	Yes - 17q21 (FRA17D)

Additional aberrations in wild-type (PD ~200)

inv(16)(p11.2q23)	Yes - 16q23	Yes - 16q23.2 (FRA16D)	Yes - 16q23.2 (FRA16D)
der(3)t(3;14)(q27;q11.2)	Yes - 3q27	Yes - 3q27 (FRA3C)	Yes - 3q27 (FRA3C), 14q11.1 (FRA14D)

Additional aberrations in *MCM10+/-* #8 (PD ~25)

t(5;8)(p15;q13)	No	No	Yes - 5p15 (FRA5H); 8q13 (FRA8F)
i(21)(q10)	No	No	No
der(1)t(1;10)(q21;q11.2)	Yes - 1q21.1;10q11.2	Yes - 1q21 (FRA1F); 10q11.2 (FRA10G)	Yes - 1q21 (FRA1F); 10q11.2 (FRA10G)
der(10)t(1;10)(q21;q11.2)	Yes - 1q21.1;10q11.2	Yes - 1q21 (FRA1F); 10q11.2 (FRA10G)	Yes - 1q21 (FRA1F); 10q11.2 (FRA10G)
der(5)t(5;10)(p15;q22)	Yes - 10q22.1	Yes - 10q22.1 (FRA10D)	Yes - 5p15 (FRA5H); 10q22.1 (FRAD10D)
der(10)t(5;10)dup(10)	No	No	No
del(11)(p11.2)	No	No	Yes - 11p11.2 (FRA11L)
del(11)(q23)	Yes - 11q23.3	Yes - 11q23.3 (FRA11B/FRA11G)	Yes - 11q23.3 (FRA11G)
dup(7)(q22q32)	Yes - 7q22,7q32.3 (FRA7H)	Yes - 7q22 (FRA7F), 7q31.2 (FRA7H)	Yes - 7q22 (FRA7F), 7q32.3 (FRA7H)
del(13)(q22q34)	Yes - 13q32	Yes - 13q32 (FRA13D)	Yes - 13q22 (FRA13E), 13q31 (FRA13H, 13q32 (FRA13D), 13q34 (FRA13I)
del(1)(q32q42)	Yes - 1q41.1	No	Yes - 1q32 (FRA1Q), 1q41 (FRA1R), 1q42 (FRA1H)
add(15)(p11.2)	No	No	No

Additional aberrations in *MCM10+/-* #8 (PD ~100)

del(6)(q16)	No	No	Yes - 6q16.3 (FRA6J)
i(15)(q10)	No	No	No
del(2)(q23)	No	No	Yes - 2q23 (FRA2S)
add(10)(p11.2)	No	No	Yes - 10p11.2 (FRA10J)
del(11)(p11.2)	No	No	Yes - 11p11.2 (FRA11L)
add(3)(q21)	No	No	Yes - 3q21 (FRA3M)
del(5)(q13)	No	No	Yes - 5q13 (FRA5K)
del(11)(q13)	No	Yes - 11q13 (FRA11H)	Yes - 11q13.3 (FRA11H)
add(12)(p11.2)	No	No	Yes - 12p11.2 (FRA12H)
idic(6)(p23~25)	Yes - 6p25	Yes - 6p23 (FRA6A), 6p25.1 (FRA6B)	Yes - 6p23 (FRA6A), 6p25.1 (FRA6B)
del(2)(q31)	Yes - 2q31 (FRA2G)	Yes - 2q31 (FRA2G)	Yes - 2q31 (FRA2G)
idic(15)p12	No	No	No

del(3)(p11.2)	No	No	No
add(19)(p13)	No	Yes - 19p13 (FRA19B)	Yes - 19p13.1 (FRA19B)
dic(18;22)(p11.2;p11.2)	No	No	No
add(17)(q25p11.2)	No	No	Yes - 17q25 (FRA17E), 17p11 (FRA17C)
dic(14;15)(q32;q23~26)	No	No	Yes - 14q32 (FRA14H), 15q24 (FRA15), 15q25 (FRA15F), 15q26 (FRA15G)
add(17)(q25)	No	No	Yes - 17q25 (FRA17E)
del(13)(q32)	Yes - 13q32	Yes - 13q32 (FRA13D)	Yes - 13q32 (FRA13D)
t(14;15)(q22;p11)	No	No	Yes - 14q22 (FRA14F)
add(20)(p11.2)	No	No	Yes - 20p11.23 (FRA20A)
inv(4)(p14;q31)	Yes - 4q31.1	Yes - 4q31.1 (FRA4C)	Yes - 4p14 (FRA4G), 4q31.1 (FRA4C)
der(5)t(5;8)del(5)(q31)	No	No	Yes - 5q31.1 (FRA5C)
del(6)(q16)	No	No	Yes - 6q16.3 (FRA6J)
Overlap of *MCM10+/-* #8 aberrations with CFSs	**31% (11/35)**	**34% (12/35)**	**80% (28/35)**

Table 1. Overlap of novel chromosomal aberrations in HCT116 wild-type and *MCM10+/-* #8 cell lines with common fragile sites. List of expected and novel chromosomal aberrations identified in HCT116 wild-type or *MCM10* mutant karyotypes.